LETTER

Lunar true polar wander inferred from polar hydrogen

M. A. Siegler[1,2]*, R. S. Miller[3]*, J. T. Keane[4]*, M. Laneuville[5], D. A. Paige[6], I. Matsuyama[4], D. J. Lawrence[7], A. Crotts[8]‡ & M. J. Poston[9]

The earliest dynamic and thermal history of the Moon is not well understood. The hydrogen content of deposits near the lunar poles may yield insight into this history, because these deposits (which are probably composed of water ice) survive only if they remain in permanent shadow. If the orientation of the Moon has changed, then the locations of the shadowed regions will also have changed. The polar hydrogen deposits have been mapped by orbiting neutron spectrometers[1–3], and their observed spatial distribution does not match the expected distribution of water ice inferred from present-day lunar temperatures[4,5]. This finding is in contrast to the distribution of volatiles observed in similar thermal environments at Mercury's poles[6]. Here we show that polar hydrogen preserves evidence that the spin axis of the Moon has shifted: the hydrogen deposits are antipodal and displaced equally from each pole along opposite longitudes. From the direction and magnitude of the inferred reorientation, and from analysis of the moments of inertia of the Moon, we hypothesize that this change in the spin axis, known as true polar wander, was caused by a low-density thermal anomaly beneath the Procellarum region. Radiogenic heating within this region resulted in the bulk of lunar mare volcanism[7–11] and altered the density structure of the Moon, changing its moments of inertia. This resulted in true polar wander consistent with the observed remnant polar hydrogen. This thermal anomaly still exists and, in part, controls the current orientation of the Moon. The Procellarum region was most geologically active early in lunar history[7–9], which implies that polar wander initiated billions of years ago and that a large portion of the measured polar hydrogen is ancient, recording early delivery of water to the inner Solar System. Our hypothesis provides an explanation for the antipodal distribution of lunar polar hydrogen, and connects polar volatiles to the geologic and geophysical evolution of the Moon and the bombardment history of the early Solar System.

Lunar polar volatiles, including water ice, record the delivery, weathering and loss of external material, as well as the orbital dynamic history of the Moon[4,12,13]. Epithermal neutron deficits measured by orbital instruments provide an effective means of probing the spatial distribution and quantity of these volatiles through the measurement of hydrogen abundances. Here, we use improved data sets of lunar hydrogen abundance that are derived using a statistics-based likelihood analysis[14–16], shown in Fig. 1a, b. Our analysis relies on data from the Lunar Prospector Neutron Spectrometer (see Methods for a discussion of additional neutron data sets). Enhancements are determined on a pixel-by-pixel basis relative to the mid-latitude lunar highlands, which are assumed to be hydrogen-poor[14,16]. Modelled present-day temperature-dependent ice stability depths are also shown at the approximate spatial resolution of the Lunar Prospector Neutron Spectrometer (Fig. 1c, d).

These maps show four key features: first, the polar hydrogen maxima (north: 84.9° N, 147.9° E; south: 84.1° S, 309.4° E) are offset from the current rotation axis of the Moon by roughly 5.5°; second, the hydrogen enhancements are of similar magnitude at both poles; third, the asymmetric enhancements do not correlate with expectations from the current thermal or permanently shadowed environment[4,5,17]; and fourth, and most relevant to this study, the spatial distributions of polar hydrogen appear to be nearly antipodal.

A perfect antipodal relationship would manifest as identical distributions separated by 180° in longitude (Methods, Extended Data Fig. 1). This relationship can be quantified for any set of north–south spatial distributions by calculating $r(\alpha=0)$ and $r(\alpha)$, where $r(\alpha)$ is the correlation coefficient obtained when the south polar distribution is rotated by an angle α in longitude relative to the north polar distribution (Fig. 2a). Figure 2b, c shows the correlation $r(\alpha)$ and the significance of that correlation $P(\alpha)$ (see Methods) for polar hydrogen, the modelled ice stability depths and the maximum and average yearly temperatures measured by Lunar Reconnaissance Orbiter Diviner[5]. Only hydrogen shows statistically significant correlations ($>5\sigma$), with peak significance near $\alpha=180°$ (8.3σ at 187°).

The unique, high-significance antipodal relationship suggests a fundamental connection between north and south polar hydrogen. We interpret this as evidence that the lunar spin axis has reoriented from a past spin pole position, with the expectation that volatiles will accumulate in cold traps about the instantaneous poles. Our 'palaeopole' is described by the averaged polar hydrogen maxima, corresponding to 84.5° N, 138° E in the north (84.5° S, 318° E in the south). Models of ice stability that assume an admixture of thermal environments from the current and palaeopole orientations (Fig. 1e, f) lead to a better description of the hydrogen distributions than does the current environment alone (see Methods).

This type of reorientation is known as true polar wander (TPW). In a minimum energy state, the spin axis of a planet will align with the maximum principal axis of inertia. TPW results when the maximum principal axis changes orientation owing to mass redistribution within the planet[18] (see Methods). As the principal axis changes, the planet will attempt to minimize rotational energy and reorient to align this principal axis with the spin axis. This reorientation results in motion of the spin axis with respect to the surface of the planet (although the spin axis remains fixed in inertial space). Lunar TPW of varying age, magnitude and direction has been previously suggested on the basis of topography, gravity and remnant magnetism[19–21] (see Methods); however, polar volatiles have not previously been used to infer polar wander on the Moon.

A palaeo-axis represents a previous maximum principal axis of inertia. Because the present-day lunar inertia tensor is known, we can test whether a single mass anomaly could reorient the Moon from the neutron-data-derived palaeo-axis to the present-day spin axis. Using a
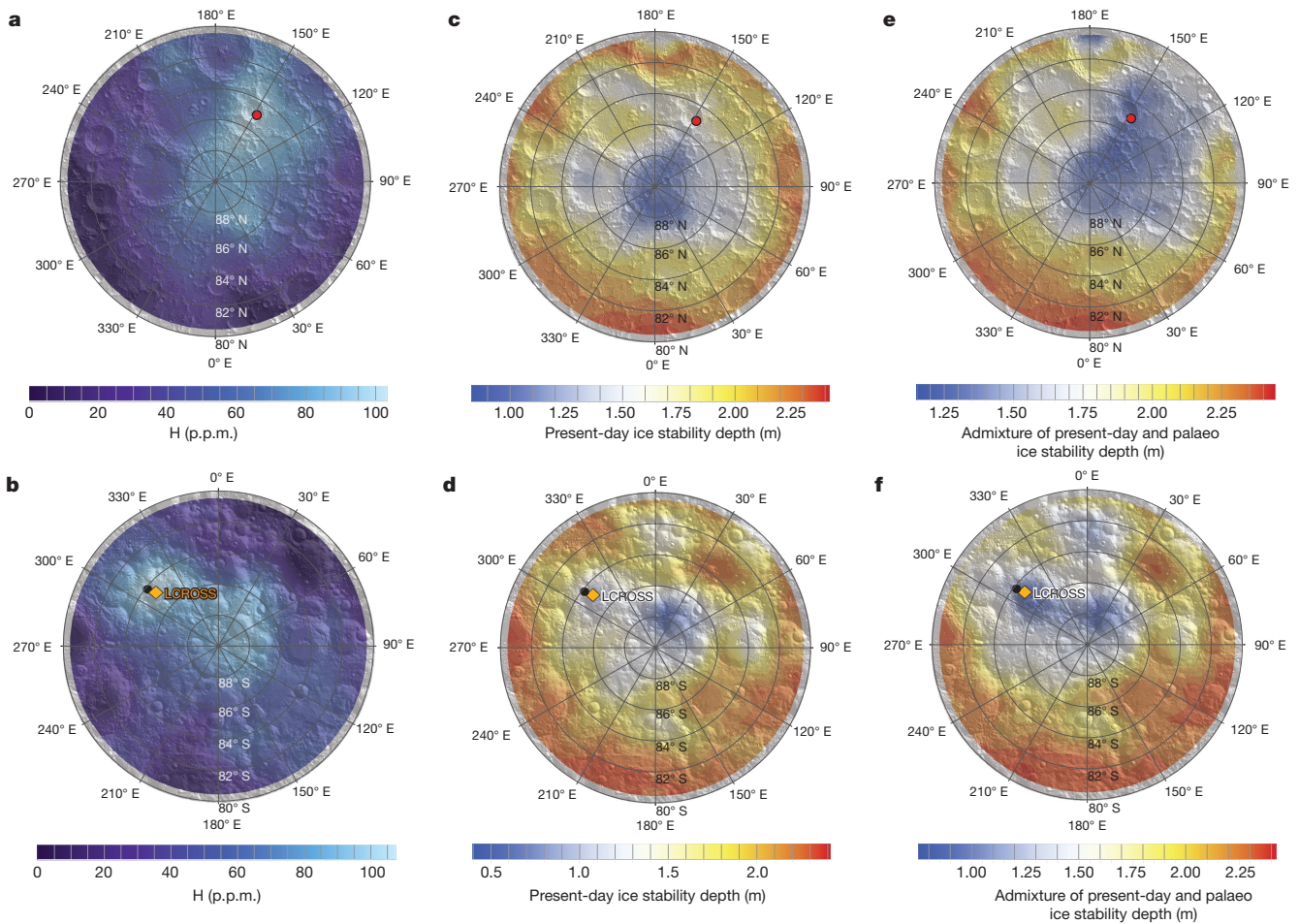
Figure 1 | Lunar polar hydrogen and predicted ice stability fields.
a, b, Abundance enhancements of lunar polar hydrogen (H; given in p.p.m.) for the north (**a**) and south (**b**) poles[15,17]. **c–f,** Ice stability depths for the north (**c, e**) and south (**d, f**). Depths for the current epoch (**c, d**), and an admixture of current and palaeopole epochs (**e, f**) are shown separately.

Ice stability depths are based on the model described in refs 5 and 6. In all panels, the red and black filled circles show the locations of the northern and southern hydrogen enhancement maximums, respectively, and the orange diamond shows the LCROSS impact site. All maps show quantities poleward of 80° with markers every 2°.
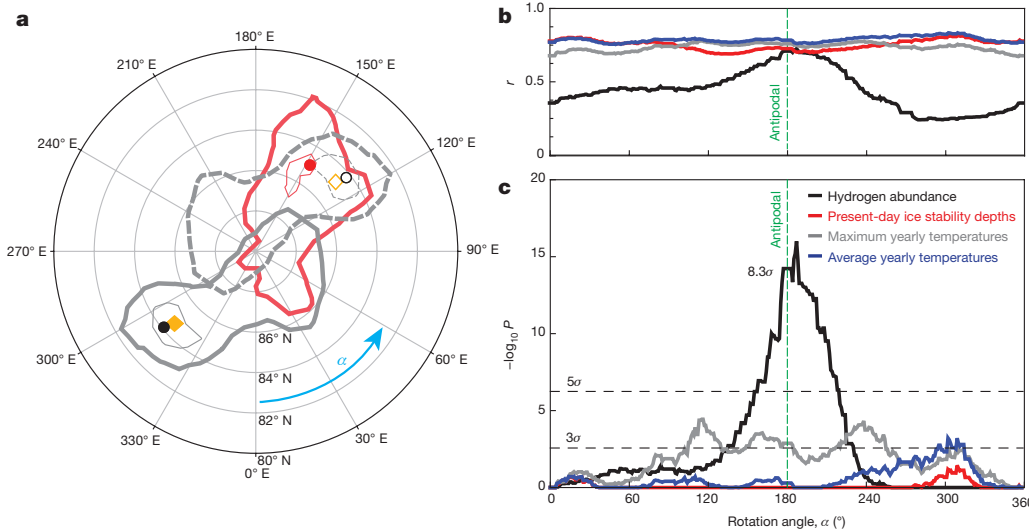

Figure 2 | Antipodal nature of polar hydrogen. a, Hydrogen abundance contours at 75 p.p.m. (thick) and 100 p.p.m. (thin) as viewed from the north pole. North (red) and south (grey; solid $\alpha = 0°$, dashed $\alpha = 180°$) spatial distributions are shown poleward of 80° with markers every 2°. The red filled circle shows the northern hydrogen enhancement maximum, the black filled circle shows the southern maximum and the filled diamond shows the LCROSS impact site; open shapes are projections onto the north. **b, c,** Computed correlation coefficients $r(\alpha)$ (**b**) and probability values $-\log_{10}(P)$ (**c**) versus longitudinal rotation angle α, for hydrogen abundances (black), current ice stability depths (red), and maximum (grey) and average (blue) yearly temperatures. High values of $-\log_{10}(P)$ represent low-chance probabilities. Reference significance values at 3σ and 5σ are also shown (horizontal dashed lines). The maximum correlation is found to have 8.3σ significance.
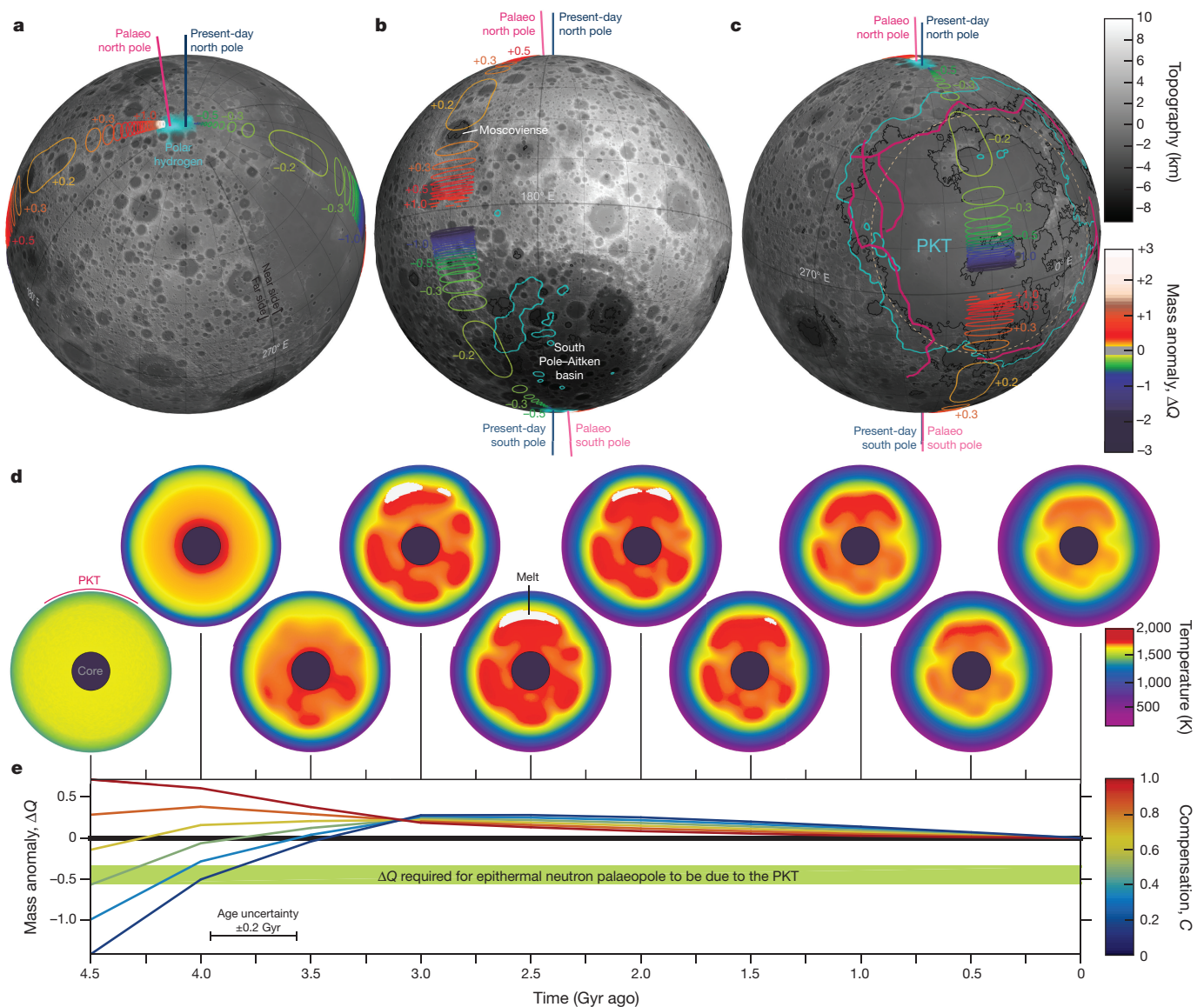
Figure 3 | The locations of plausible mass anomalies that produce the required TPW, and the effect of the PKT. a–c, Orthographic spherical projection of the lunar northern hemisphere (**a**), far side (**b**) and near side (**c**), with contours enclosing the locations where mass anomalies ΔQ of the indicated size must be centred to reorient the Moon from the epithermal neutron palaeo-axis (pink lines) to the present-day spin axis (dark blue lines). Positive mass anomalies ($\Delta Q > 0$) indicate present-day mass excesses; negative mass anomalies ($\Delta Q < 0$) indicate present-day mass deficits. Our preferred solution is a negative mass anomaly beneath the PKT (dashed tan circle and dot). For reference, LRO/LOLA (Lunar Reconnaissance Orbiter/Lunar Orbiter Laser Altimeter) topography[29]

(grey-scale), mare basalts boundaries from LRO/WAC (Wide Angle Camera) mapping (black lines, data available at http://wms.lroc.asu.edu/lroc/view_rdr/SHAPEFILE_LUNAR_MARE), the PKT as identified by a 3.5-p.p.m. thorium contour[30] (cyan contours) and the PKT-border gravity anomalies[11] (pink lines) are also shown. **d, e**, 2D cross-sections (**d**) of 3D thermochemical convection models from model W of ref. 9 that was used to determine the effective mass anomaly (**e**) associated with the PKT for different values of lithospheric compensation C. $C = 0$ corresponds to a rigid lithosphere; $C = 1$ corresponds to a strengthless lithosphere. This evolution is also illustrated in Supplementary Video 1.

parameter-space search, positive and negative mass anomalies of varying size were placed across the lunar surface, and changes to the lunar inertia tensor were evaluated. Reorientation in response to these mass anomalies is counteracted by the Moon's non-equilibrium degree-2 figure[21].

Figure 3a–c shows the regions in which a mass anomaly $\Delta Q = J_2^{MA}/J_2$ (in which $J_2^{(MA)}$ is the degree-2 zonal spherical harmonic gravity coefficient without (with) the addition of a mass anomaly; see Methods) of a given magnitude would cause a reorientation of the Moon from within 1° of the hypothesized palaeo-axis to the present-day spin axis. Both positive (mass excesses; $\Delta Q > 0$) and negative (mass deficits; $\Delta Q < 0$) anomalies are possible, although the allowed regions are limited. These regions depend only on the observed lunar

inertia tensor and the location of the palaeopoles. To first order, anomalies fall on large circles connecting the present-day poles and the palaeopoles (Fig. 3a), although they deviate owing to the triaxial nature of the Moon.

Although many impact basins fall within the allowed regions, inverse modelling of the gravity fields of lunar impact basins shows that most do not have a large enough mass anomaly to produce the required reorientation[21]. Only the South Pole–Aitken basin has a large enough mass anomaly, but does not correlate with any of the allowed regions and would result in roughly orthogonal motion to our proposed wander path (Extended Data Fig. 8e).

The centre of the radiogenic-rich Procellarum KREEP Terrane (PKT; a region rich in potassium, rare-earth elements and phosphorous[7]) lies

a Rigid lithosphere, $C = 0$

b Partially rigid lithosphere, $C = 0.5$

c Strengthless lithosphere, $C = 1$

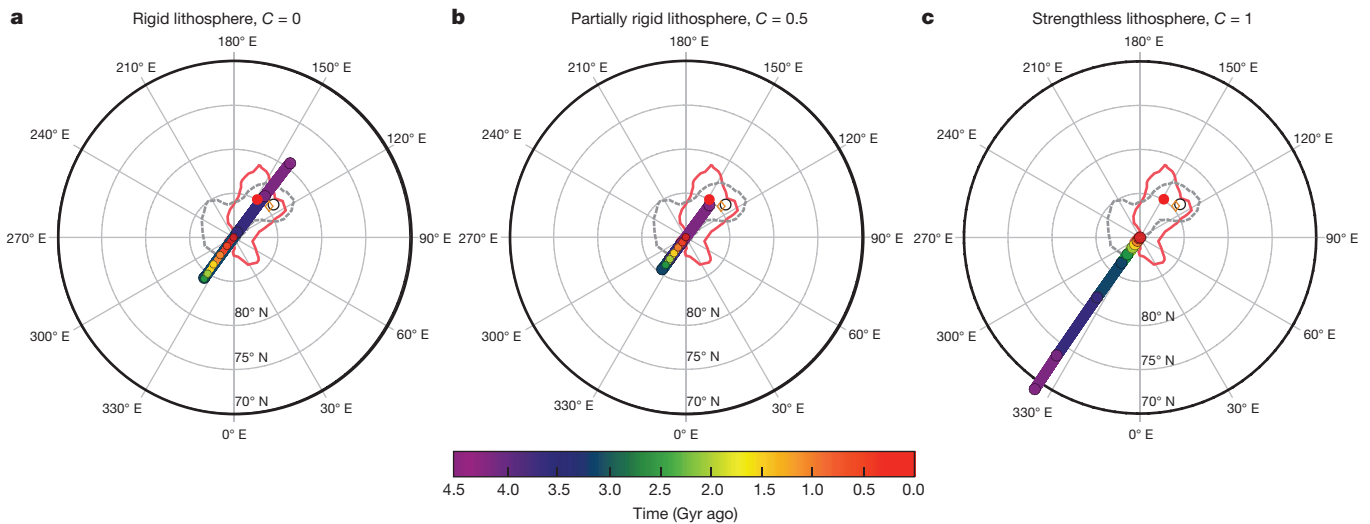Time (Gyr ago)
4.5 4.0 3.5 3.0 2.5 2.0 1.5 1.0 0.5 0.0

Figure 4 | TPW due to the evolution of the PKT. a–c, The predicted TPW path backwards through time from the present-day pole (red), owing to the thermal evolution of the PKT, for a model with KREEP material mixed within the crust (model W), assuming a rigid lithosphere ($C = 0$; **a**), a partially rigid lithosphere ($C = 0.5$; **b**) and a strengthless lithosphere ($C = 1$; **c**). In **a** and **b**, the TPW paths pass through the palaeopole, which is not forced by the model. The 1σ uncertainty in pole position due to the rotational ambiguity of the PKT thermal anomalies are smaller than the plotted points. Other features are as in Fig. 2a.

within the acceptable regions (Fig. 3c). The thermal evolution of the PKT has previously been used to explain the formation of the near-side mare basalts, the distributions of incompatible elements, the anomalous heat flow and the gravity signature of the PKT[7–11,22,23]; however, the effect of PKT thermal evolution on the moments of inertia of the Moon has not been examined. A simple model of the PKT as a spherical internal mass anomaly that spans the mantle requires only a moderate density anomaly ($|\Delta\rho| > 15\,\mathrm{kg\,m^{-3}}$; equivalent to a temperature anomaly of $|\Delta T| > 150\,\mathrm{K}$) to generate the required reorientation (see Methods). This anomaly is similar in magnitude to the thermal anomalies suggested to sit beneath the PKT[7–11,22,23].

To determine whether the thermal evolution of the PKT can produce the required reorientation, we use the 3D thermochemical convection model of ref. 9. This model (Fig. 3d) evaluates the influence of the high concentration of heat sources within the PKT on global thermal evolution. Two limiting models are considered here: heat-producing KREEP material initially beneath the crust (model 'B'), and heat-producing KREEP material initially mixed within the crust (model 'W'); see Methods. Using these models, we evaluate changes in the lunar inertia tensor and, hence, in the spin axis, as functions of time. These changes are caused by internal density variations as a result of temperature and compositional changes, and surface deformation. Figure 3e shows the mass anomaly ΔQ of our nominal PKT thermal evolution model (model W) as a function of time, for a range of lithospheric compensation states C. All PKT thermal evolution models produce substantial perturbations to the lunar inertia tensor, and large amounts of TPW, regardless of model parameters or compensation state (Extended Data Figs 9, 10). Models with semi-rigid lithospheres ($C < 0.5$) produce mass anomalies that are consistent with those required for PKT to be responsible for the reorientation implied by our palaeopole ($\Delta Q = -0.45$; Fig. 3c).

Figure 4 shows the chronology of three representative TPW paths derived using the nominal PKT thermal evolution for different lithospheric strengths. Starting from the present-day (non-equilibrium) lunar inertia tensor and working backwards in time allows us to track TPW due to PKT thermal evolution without making assumptions about the lunar fossil figure. TPW tracks are not forced to pass through the epithermal neutron palaeopoles; this is simply a result of placing the thermal anomaly within the PKT. As long as the lithosphere is moderately rigid, tracks will pass through the palaeopole (Fig. 4a, b, Extended

Data Figs 9, 10). This result is consistent with the present geophysical state of the PKT[9] and expectations of the early rigid lunar lithosphere[24]. TPW tracks assuming a strengthless lithosphere ($C \approx 1$) do not pass through the palaeopole (Fig. 4c, Extended Data Figs 9, 10), constraining past lithospheric compensation.

Although the allowed locations and magnitudes of perturbing mass anomalies are robust (Fig. 3a–c, Extended Data Fig. 7), other geophysical processes can affect our proposed TPW, owing to the degeneracy of interpreting gravity and moments of inertia. The TPW paths and chronology depend sensitively on the compensation state of the lithosphere and on the emplacement and relaxation of near-side mare basalts. Future seismic and heat-flow measurements will constrain the current nature of the PKT thermal anomaly. Passage through the palaeopole occurs more than 3.5 Gyr ago for these representative models. Alternative chronologies that incorporate early magma-ocean evolution, mare emplacement and changes in lithospheric strength may lead to later palaeopole passage, but require additional free parameters and modelling (Extended Data Fig. 10).

Because a substantial fraction of the observed hydrogen deposits are believed to record an ancient palaeopole, they may preserve water from the early Solar System, necessitating long-term hydrogen stability. If Mercury's polar volatiles are also ancient, then lunar TPW may explain the differences between the volatile reservoirs on these two bodies (see Methods). For many TPW scenarios, the pole may not migrate substantially, water ice may always be stable in the observed locations and the detected hydrogen could simply be the remaining ice (Extended Data Fig. 3e, f), kept near to the surface by thermal migration despite impact gardening[4,13,25]. The detection of water ice near the southern palaeopole by the Lunar Crater Observation and Sensing Satellite (LCROSS) may favour this explanation[26]. If, instead, the Moon underwent a large amount of TPW, then the palaeopole may have been directly illuminated, resulting in temperatures too high for water ice. In this scenario, surficial water adsorption[27] and storage of hydrogen within grains[28] are viable mechanisms for long-term hydrogen storage (see Methods), although the spatial distribution would still point to a pre-TPW deposition in the form of ice. *In situ* measurements, sample return and high-resolution orbital geochemistry measurements could differentiate plausible TPW scenarios.

1. Feldman, W. C. *et al.* Fluxes of fast and epithermal neutrons from Lunar Prospector: evidence for water ice at the lunar poles. *Science* **281,** 1496–1500 (1998).
2. Feldman, W. C. *et al.* Evidence for water ice near the lunar poles. *J. Geophys. Res.* **106,** 23231–23251 (2001).
3. Mitrofanov, I. G. *et al.* Hydrogen mapping of the lunar south pole using the LRO neutron detector experiment LEND. *Science* **330,** 483–486 (2010).
4. Siegler, M. A., Paige, D., Williams, J.-P. & Bills, B. Evolution of lunar polar ice stability. *Icarus* **255,** 78–87 (2015).
5. Paige, D. A. *et al.* Diviner lunar radiometer observations of cold traps in the Moon's south polar region. *Science* **330,** 479–482 (2010).
6. Paige, D. A. *et al.* Thermal stability of volatiles in the north polar region of Mercury. *Science* **339,** 300–303 (2013).
7. Jolliff, B. L., Gillis, J. J., Haskin, L. A., Korotev, R. L. & Wieczorek, M. A. Major lunar crustal terranes: surface expressions and crust-mantle origins. *J. Geophys. Res. Planets* **105,** 4197–4216 (2000).
8. Wieczorek, M. A. & Phillips, R. J. The "Procellarum KREEP Terrane": implications for mare volcanism and lunar evolution. *J. Geophys. Res. Planets* **105,** 20417–20430 (2000).
9. Laneuville, M., Wieczorek, M. A., Breuer, D. & Tosi, N. Asymmetric thermal evolution of the Moon. *J. Geophys. Res. Planets* **118,** 1435–1452 (2013).
10. Grimm, R. E. Geophysical constraints on the lunar Procellarum KREEP Terrane. *J. Geophys. Res. Planets* **118,** 768–778 (2013).
11. Andrews-Hanna, J. C. *et al.* Structure and evolution of the lunar Procellarum region as revealed by GRAIL gravity data. *Nature* **514,** 68–71 (2014).
12. Arnold, J. R. Ice in the lunar polar regions. *J. Geophys. Res. Solid Earth* **84,** 5659–5668 (1979).
13. Hurley, D. M. *et al.* Two-dimensional distribution of volatiles in the lunar regolith from space weathering simulations. *Geophys. Res. Lett.* **39,** L09203 (2012).
14. Miller, R. S., Nerurkar, G. & Lawrence, D. J. Enhanced hydrogen at the lunar poles: new insights from the detection of epithermal and fast neutron signatures. *J. Geophys. Res. Planets* **117,** E11007 (2012).
15. Miller, R.S. Statistics for orbital neutron spectroscopy of the Moon and other airless planetary bodies. *J. Geophys. Res. Planets* **117,** E00H19 (2012).
16. Miller, R. S., Lawrence, D. J. & Hurley, D. M. Identification of surface hydrogen enhancements within the Moon's Shackleton crater. *Icarus* **233,** 229–232 (2014).
17. Teodoro, L. F. A., Eke, V. R. & Elphic, R. C. Spatial distribution of lunar polar hydrogen deposits after KAGUYA (SELENE). *Geophys. Res. Lett.* **37,** L12201 (2010).
18. Matsuyama, I., Nimmo, F. & Mitrovica, J. X. Planetary reorientation. *Annu. Rev. Earth Planet. Sci.* **42,** 605–634 (2014).
19. Takahashi, F., Tsunakawa, H., Shimizu, H., Shibuya, H. & Matsushima, M. Reorientation of the early lunar pole. *Nature Geosci.* **7,** 409–412 (2014).
20. Garrick-Bethell, I., Perera, V., Nimmo, F. & Zuber, M. T. The tidal–rotational shape of the Moon and evidence for polar wander. *Nature* **512,** 181–184 (2014).
21. Keane, J. T. & Matsuyama, I. Evidence for lunar true polar wander and a past low eccentricity, synchronous lunar orbit. *Geophys. Res. Lett.* **41,** 6610–6619 (2014).
22. Zhong, S., Parmentier, E. M. & Zuber, M. T. A dynamic origin for the global asymmetry of lunar mare basalts. *Earth Planet. Sci. Lett.* **177,** 131–140 (2000).
23. Zhang, N., Parmentier, E. M. & Liang, Y. A 3D numerical study of the thermal evolution of the Moon after cumulate mantle overturn: the importance of rheology and core solidification. *J. Geophys. Res. Planets* **118,** 1789–1804 (2013).
24. Zhong, S. & Zuber, M. T. Long-wavelength topographic relaxation for self-gravitating planets and implications for the time-dependent compensation of surface topography. *J. Geophys. Res. Planets* **105,** 4153–4164 (2000).
25. Schorghofer, N. & Taylor, G. J. Subsurface migration of H_2O at lunar cold traps. *J. Geophys. Res. Planets* **112** E02010 (2007).
26. Colaprete, A. *et al.* Detection of water in the LCROSS ejecta plume. *Science* **330,** 463–468 (2010).
27. Poston, M. J. *et al.* Temperature programmed desorption studies of water interactions with Apollo lunar samples 12001 and 72501. *Icarus* **255,** 24–29 (2015).
28. Starukhina, L. in *Moon: Prospective Energy and Material Resources* (ed. Badescu, V.) 57–85 (Springer, 2012).
29. Smith, D. E. *et al.* Initial observations from the Lunar Orbiter Laser Altimeter (LOLA). *Geophys. Res. Lett.* **37** L18204 (2010).
30. Lawrence, D. J. *et al.* Small area thorium features on the lunar surface. *J. Geophys. Res. Planets* **108,** 5102 (2003).

METHODS

Determination of hydrogen abundance. Orbital neutron spectroscopy is commonly divided into three distinct energy regimes—thermal (low energy), epithermal (intermediate energy) and fast (high energy)—each providing complimentary information about elemental abundance and distribution (spatial and depth). The process starts with fast neutrons created by cosmic-ray interactions in the lunar regolith. Elastic neutron–proton scattering causes these neutrons to rapidly lose energy, shifting some of them into the epithermal regime. Subsequent moderation and/or capture processes can further modify the flux and spectrum thereby imprinting details of the intervening material on escaping neutrons. Owing to the efficiency of the neutron energy-loss process, the epithermal regime is an especially sensitive probe of hydrogen[1,2]. Epithermal neutron deficits measured from orbit are therefore indicative of enhanced hydrogen abundances.

Proper determination of statistical significance is often exchanged for approximate methods that may be simple or reduce computation requirements. Low signal-to-noise environments require a more rigorous approach. Relevant statistical descriptions are based on particle counts, not rates, and therefore require the use of exposure distributions in addition to observed neutron count rates. Our statistical analysis approach uses a likelihood parameter λ to characterize consistency between acquired neutron data and a hydrogen-poor (null) hypothesis on a pixel-by-pixel basis. This parameter incorporates fundamental observational details as well as the inherent uncertainties associated with counting statistics. The likelihood parameter is governed by a well-known statistical distribution (χ^2) and, hence, can be used to exclude features of low or marginal significance. The null hypothesis is rejected, on a pixel-by-pixel basis, if λ exceeds a predetermined critical value. For this work the critical value ($\lambda = 25$) was chosen to correspond to a chance probability of 5.7×10^{-7}, equivalent to a 5σ Gaussian detection with 1 degree of freedom. Additional details of the statistical analysis framework used here are found in ref. 15.

Significance maps are converted to hydrogen abundance distributions following the procedure outlined in ref. 14 (and references therein). Briefly, the statistical significance (for example, λ-statistic) is proportional to the magnitude of neutron count rate deficits, which in turn correlates directly with hydrogen abundance[1]. The relationship between neutron count rates and hydrogen abundances has been derived using Monte Carlo simulations that assume that the regolith has a composition equivalent to ferroan anorthosite[1]. Hydrogen abundance distributions for Lunar Prospector (LP), obtained following the likelihood-based analysis protocols described above, are shown in Fig. 1.

Additional neutron data sets. The Lunar Reconnaissance Orbiter (LRO) Lunar Exploration Neutron Detector (LRO/LEND) includes a combination of collimated and uncollimated ^{3}He sensors[3,31,32] with one of the four uncollimated sensors configured for epithermal neutron detection. The collimated sensors for epithermal neutrons (CSETN) were designed to provide data with improved spatial resolution over uncollimated sensors, but low count rates and systematic background effects limit its value for confidently inferring hydrogen concentrations with high spatial resolution[14,33–36]. Because of these documented problems, the collimated LEND data are not used in this study. Uncollimated epithermal neutron data from the LEND sensors for epithermal neutrons (SETN) have been shown to have a reasonably good spatial correlation with the uncollimated LP data[14,32]. The correlations between the two uncollimated data sets, however, are not perfect, and at best only qualitative suggestions have been provided to explain discrepancies that occur in both equatorial and polar regions[32]. Similar to LP, the spatial distribution of hydrogen derived from LEND-SETN does not match the predicted locations of water ice in the present thermal environment, and shows a broad, asymmetric, slightly off-polar distribution[32]. However, there are quantitative differences between LEND and LP that are not fully understood or documented. Our confidence in the LP data is well grounded because the LP data were measured with well-characterized sensors on a boom such that backgrounds from nearby materials were both understood and minimized[37], and because the data reduction is supported by extensive documentation[38] and a well-validated comparison with modelled count rates[39]. We expect that a more detailed analysis of the LEND data could provide additional insight to the differences between these data sets. However, such an analysis is beyond the scope of this study, and we have therefore focused on the LP-derived parameters.

Antipodal symmetry. Two surface features are antipodal if they lie on diametrically opposite sides of a planet, such that a line connecting the two points passes through the centre of the planet. If a feature has a latitude and longitude of (θ, φ), then the antipode is located at ($-\theta, \varphi + 180°$). This type of symmetry can also be referred to as an inversion, central reflection or point reflection.

In typical map projection of polar data sets (for example, Fig. 1), antipodal features do not appear simply shifted by 180°. The different handedness between the north and south polar maps results in an additional reflection. This geometry

is illustrated schematically in Extended Data Fig. 1a and b, in which two antipodally symmetric features are shown in north and south polar maps, respectively. To illustrate the antipodal nature of this feature, we show both north and south features in each plot, with the antipodal feature shown as it would appear if you could view it through the Moon. In this projection, a feature rotated by an angle (α) of 180° about the pole will exactly line up with its antipodal self (Extended Data Fig. 1c, d).

Correlation analysis. The Pearson product-moment correlation coefficient r is used to quantify the strength of the correlations between data sets[40]. Values of this statistic occur within limits ($-1 \le r \le 1$) corresponding to perfect anti-correlation and correlation, respectively. A two-point correlation was implemented to operate on pixelated spatial distributions characterized by latitude and longitude. This coefficient measures similarities in relative amplitude (or shape) only, and is not used to evaluate the physics implications of the absolute neutron rates or thermal parameters.

By itself the correlation coefficient is not a good statistic for determining the quality of an observed correlation. However, the significance of differences in correlation coefficients is relevant. The Fisher z-transformation facilitates hypothesis testing by quantifying whether a change in some physical parameter modifies the baseline correlation between two distributions. When applied to the Pearson coefficient it stabilizes the variance[41] and can be used to determine significance. Fisher's transformation takes the form

$$z(r) = \frac{1}{2} \ln\left(\frac{1+r}{1-r}\right) \tag{1}$$

and has a standard error of

$$\sigma(z) \approx \frac{1}{\sqrt{N-3}}$$

where N is the number of measurements in the population. If the baseline correlation (or null hypothesis) is characterized by a coefficient r_0 and a second correlation by r, then the two-sided significance of the difference between the two measured coefficients ($\Delta z = |z(r_0) - z(r)|$) is

$$P = \mathrm{erfc}\left(\frac{\Delta z \sqrt{N-3}}{\sqrt{2}}\right) \tag{2}$$

where erfc(x) is the complementary error function[41]. The Fisher transformation also enables determination of confidence levels. Because z can be approximated by a normal distribution with known variance, a 90% confidence interval is given by

$$z - 1.64\sigma(z) \le z \le z + 1.64\sigma(z)$$

and application of the inverse Fisher transform yields the relevant confidence intervals on the measured correlation coefficient r.

The determination of significance assumes that polar map pixels are independent. A globally mapped, equal-area pixel size was selected to match the ~45-km spatial resolution of acquired neutron data[14], but total independence cannot be assured. This results in each polar region containing 364 equal-area pixels. Of those, only 248 (123 in the north and 125 in the south) meet the statistical threshold requirement discussed below ($\lambda = 25$). The number of pixels (N) used to evaluate significance was independent for each α and includes only those pixels common to the unrotated case ($\alpha = 0°$); at peak significance $N = 236$.

Using equation (1), the peak in Fig. 2b corresponds to $\Delta z = 0.548$ (with $r = 0.728$ and $r_0 = 0.356$). Substituting these values into equation (2), we obtain $-\log_{10}(P) = 16.2$, which corresponds to the peak in Fig. 2c and is equivalent to about 8.3σ. Even if the spatial distributions are oversampled by a factor of two—an extreme exaggeration that reduces the number of pixels to $N = 118$—the observed antipodal correlation is still significant, with a chance probability $< 10^{-9}$, which exceeds a 5σ threshold.

Random processes (noise) will degrade any observed correlations. Therefore, investigating the dependence of inter-polar correlations on the likelihood parameter λ is instructive because it serves as a proxy for statistical significance of features. North and south polar hydrogen distributions show evidence for a strong near-antipodal relationship. Extended Data Fig. 2 shows peak significance $-\log_{10}(P)$ as a function of λ. A reduction in correlation significance as low-λ (low statistical significance) features are included is evident. Such a trend is expected if the features identified above the critical threshold ($\lambda \ge 25$) are real, and those below are dominated by statistical fluctuations.

Surface thermal model to examine ice stability. The central argument for the existence of lunar volatiles is based on thermal modelling[42]. The forward thermal model presented here (for example, Figs 1c, d, 3 and 4) is an updated version of

that presented in refs 5 and 6. The thermal model we use is intended to be the simplest model that can reproduce the major features of the LRO Diviner south polar observations. Updates to the model of ref. 5 include the use of polar meshes and an updated model of the Sun and its ephemeris, as detailed below.

Polar meshes were modified to reproduce thermal conditions under the assumption of a past spin by transforming the polar stereographic 'z' coordinate to appropriately represent the change in polar position. Our offset figures were created with a map shifted to have the poles at 84.5° N, 138.6° E and 84.5° S, 318.6° E, which correspond to simple averages of the two polar hydrogen maxima.

We model the Sun using a triangular mesh consisting of 128 triangles whose radiance decreases with distance from the centre of the Sun according to the solar limb darkening curve[39]. The location and distance of the Sun relative to the Moon as a function of time is determined using the DE421 JPL Planetary Ephemeris.

The full-resolution thermal-model results for ice stability depths in Fig. 1 are presented in Extended Data Fig. 3a–d. A version of Extended Data Fig. 3b has previously been published in ref. 5, but the remaining models are new. These models show where ice would be stable from sublimation at a rate of $1\,mm\,Gyr^{-1}$ assuming a regolith cover. These depths have been shown to be consistent with radar[43,44] and neutron-spectrometer-derived depths on Mercury[45].

Volatiles should collect in the most thermally stable environments—permanently shadowed regions. Using a thermal and ice stability model[4–6], the location of possible volatile reservoirs can be identified for different polar axis locations.

The model outputs for the current lunar orientation are shown in Fig. 1. To facilitate direct comparisons with the hydrogen distributions the model outputs have been degraded to a spatial resolution of 30 km from the original 0.5 km to approximate the spatial resolution of the LP Neutron Spectrometer instrument in its low-altitude orbit. Water-ice stability depths for the current orientation, the proposed palaeopole orientation and an admixture between the two (at about 30-km resolution) are shown in Extended Data Fig. 4, which repeats parts of Fig. 1 for clarity.

Admixtures of the present-day- and palaeo-axis model results (Fig. 1e, f; Extended Data Fig. 4c, f) are better correlated to the neutron data than is the present-day model alone. A given admixture is a reasonable descriptor if the corresponding correlation between it and the hydrogen distribution improves; here, statistical significance is measured relative to the correlation with a pure current spin-axis thermal model.

For the north polar region, a present-day-only model (Fig. 1c, Extended Data Fig. 4a) is excluded at the 90% confidence level and the best descriptor is a 57%–43% admixture of current- and palaeo-axis hypotheses, respectively. The south polar region (Fig. 1d, Extended Data Fig. 4d) is consistent with a pure current spin-axis hypothesis, although the optimum north pole admixture (the 57%–43% mixture) is allowed at the 90% confidence level. This strengthens the argument that the identified longitudinal bias is related to topographic and thermal effects on hydrogen.

We caution not to over-interpret the thermal analysis because it is an approximation that incorporates only two unique polar-axis locations. A more rigorous analysis must fully account for the TPW path and chronology. However, if temperature is the fundamental parameter driving volatile retention, then this approximation provides useful insights and additional support for our hypothesis of a palaeo-axis and TPW migration. Given higher-resolution neutron measurements[46] and advances in polar crater chronology[47], it may be possible to use comparisons between neutron data and crater age to help constrain the timescale of the suggested lunar TPW. If certain craters did not exist at the time of hydrogen deposition, then they will plausibly remove near-surface hydrogen-rich materials, setting a lower limit on hydrogen age. Conversely, if hydrogen is found to be associated with relatively young craters (about 2–3.5 Gyr), then it will set an upper limit on the age of hydrogen emplacement and constrain many TPW models. Evolution of lunar obliquity can also influence volatile survivability and its spatial distribution and may inform this timeline[4,12,48,49].

True polar wander. Changes in the spin axis of a planetary body fall into two categories[50–52]: changes in obliquity and true polar wander (TPW) (Extended Data Fig. 5).

The first category involves changes in the orientation of the spin axis in inertial space (that is, changing the position of the spin axis with respect to the celestial sphere), but not with respect to the surface of the planet (Extended Data Fig. 5b). In other words: the obliquity of the planet (the angle between the planet's spin axis and the planet's orbit normal) changes. Changes of this type result from external torques acting on the planet that can alter the planet's angular momentum (both in magnitude and direction). For planets, the most notable torques are tidal torques from satellites, the Sun and other planets. Precession and nutation are well-known examples of this form of spin evolution for the Earth, as are Cassini state transitions for the Moon and Mercury[53,54]. Spin evolution of this type can have large influences

on the stability of ice at the lunar poles[4,12,48,49]. In general, near-zero obliquity is required for ice stability at the poles.

The second category of changes in planetary spin axes are those that change the orientation of the spin axis with respect to the surface of the planet, but do not change the position of the spin axis in inertial space (Extended Data Fig. 5c). This reorientation of the planet with respect to the spin axis is generally referred to as TPW[18,55,56]. Changes of this type are due to changes in the mass distribution within a planet or its hydrosphere/atmosphere. Redistribution of mass within the planet alters its inertia tensor. In a minimum energy rotation state, the rotation axis will be aligned with the maximum principal axis of inertia. If the mass redistribution changes the direction of the maximum principal axis, then the planet will reorient to keep the maximum principal axis aligned with the spin axis. Thus, to an outside (inertial) observer, the surface of the body appears to reorient with respect to the spin axis and maximum principal axis of inertia—as long as the changes in the mass distribution occur slowly with respect to the free precession period of the planet. If the changes in the inertia tensor are rapid (as might happen in the aftermath of a giant asteroid impact), the planet will enter an ephemeral period of non-principal axis rotation until the planet dissipates enough energy to return to principal axis rotation[58]. For most non-catastrophic geologic processes (for example, mantle convection and isostatic relaxation of topography), it is generally safe to assume that the planet always remains in principal axis rotation. TPW has been directly measured for the Earth, in the form of periodic TPW (driven by seasonal variations in atmospheric pressure, oceanic currents and ice loading) and secular TPW (driven by post-glacial rebound and mantle convection)[50]. Beyond Earth, TPW has been inferred for a variety of planetary bodies, including the Moon[19–21,59–64], Enceladus[65,66], Europa[66–68] and Mars[69,70] (see ref. 18 for a review). Because TPW does not change the orientation of the planet's spin vector in inertial space, the instantaneous spin pole can remain a volatile cold trap (for sufficiently small obliquities).

The many palaeopoles of the Moon. Our epithermal neutron palaeopole is not the first palaeopole proposed for the Moon. Extended Data Fig. 6 summarizes all previously proposed lunar palaeopoles. Lunar palaeopoles can be subdivided into three distinct categories on the basis of the data set used to identify them: (1) palaeomagnetic poles, (2) fossil-figure poles determined from long-wavelength topography or gravity, and (3) palaeopoles inferred from the distribution of polar volatiles (proposed for the first time here). Here we summarize these methods and the associated difficulties.

The first lunar palaeopoles were inferred from orbital surveys of crustal magnetic anomalies from Apollo 15 and 16 sub-satellites[59,60], and have subsequently been measured to higher precession with Lunar Prospector[61] and Kaguya[19,63,64] observations. These magnetic anomalies can be fitted with source models of varying prescription, and a local dipole magnitude and orientation can be determined. Assuming that this local dipole is a frozen remnant from a global, body-centred core dynamo field, the geometry of this local field can be used to infer a palaeomagnetic pole (that is, the surface location where the magnetic dipole intersects the surface). Under the assumption that the dipole is aligned with spin axis of the Moon, this palaeomagnetic pole is then a record of the spin pole at the time at which the magnetic anomaly formed.

There are several difficulties with interpreting palaeomagnetic poles. First, not all magnetic anomalies trace global dynamos. Large-scale impacts generate transient magnetic fields that can be different from any core dynamo existing at that time. Many deposits associated with magnetic anomalies (particularly those associated with impact ejecta, or features antipodal to large basins) may have experienced rapid shock-remnant magnetization during these transient fields, and thus may not accurately trace a core dynamo. To determine a true magnetic palaeopole, it is necessary to identify deposits that cooled slowly, well after the dissipation of any transient field (that is, thermoremnant magnetization). Identifying these deposits is difficult, and has been done convincingly only for a few magnetic anomalies[61,64]. Although disentangling shock-remnant and thermoremnant anomalies is difficult, it is still curious that many magnetic anomalies cluster into two groups: one near the present-day spin-pole, and one in the far-side mid-latitudes[19]. The second major difficulty with interpreting palaeomagnetic poles is that they may not accurately trace the spin axis of a planet. This is the case on Earth, where the magnetic pole is misaligned with the spin pole by about 10°. Future work will need to investigate the formation and evolution of the lunar dynamo, in 3D, to determine how large of a misalignment is possible.

There have been some attempts to infer palaeomagnetic poles from analysis of remnant magnetism in samples returned from the Apollo missions. Because the original orientation of these samples is unknown, it is not possible to completely describe the field geometry at the time these samples acquired their magnetizations— however, it is possible to infer the palaeolatitude of the samples on the basis of the orientation of the remnant field with respect to the sample's magnetic fabric, which

is used as a proxy for palaeohorizontal. Analysis of multiple samples from multiple Apollo landing sites has been used to infer palaeomagnetic poles[62].

The second types of palaeopoles are those inferred from measurements of the Moon's long-wavelength topographic shape and gravitational field—the so-called 'fossil figure'. Following the Moon's formation and differentiation, the Moon was largely molten, and probably possessed a triaxial figure in equilibrium with the tidal and rotational potential of its early orbit. Eventually, the Moon cooled, and developed an elastic lithosphere capable of supporting this primordial, fossil triaxial figure over geologic time. The axis associated with the maximum principal moment of inertia of this figure would represent the palaeopole at the time that the elastic lithosphere formed. This fossil figure was preserved even as the Moon migrated to larger radial distances from Earth and the tidal and rotational potentials decreased.

Although it is possible to directly measure the Moon's present-day figure and its associated pole (quantified by degree-2 gravity and topography), it is non-trivial to measure the primordial figure. Giant impact basins (particularly the South Pole–Aitken basin) and other large-scale geologic processes alter the Moon's figure and obscure the true fossil figure. Garrick-Bethell *et al.*[20] and Keane and Matsuyama[21] have developed two different methods for isolating this fossil figure. A critical comparison of these two works is beyond the scope of this paper, but both suggest that the fossil figure has reoriented by 15°–30° (although in different directions).

Although there is substantial scatter in the lunar palaeopoles reported in the literature (Extended Data Fig. 6), future work might be able to synthesize these data sets into a cohesive history of lunar TPW. Studies of the lunar fossil figure[20,21] should provide the 'initial' spin pole of the Moon. Paleomagnetic poles probably trace the lunar pole during the subsequent 1 Gyr, when the core dynamo was active[71]. Because polar volatiles are stable only during near-zero (roughly <12°) obliquity, polar volatiles probably trace polar wander only after the highly uncertain Cassini-state transition[49]. Although polar volatiles may not be able to trace the earliest episodes of lunar TPW, they have the distinct advantage of being capable of tracing small amounts of polar wander, late in lunar history.

Identifying the mass anomaly responsible for the epithermal neutron palaeopole. Under the assumption that the epithermal neutron palaeopole (north pole: 84.9° N, 147.9° E; south pole: 84.1° S, 309.4° E) is a former rotational palaeopole, and thus a former maximum principal axis of inertia, we ask the question: what mass anomaly would be required to reorient the Moon from this palaeopole to its present-day spin pole (0° N/S)? Phrased in terms of inertia tensors, this question is equivalent to $I = I_{palaeo} + I_{MA}$, in which I is the present-day lunar inertia tensor, I_{MA} is the inertia tensor of some arbitrary mass anomaly and I_{palaeo} is an undetermined inertia tensor with the maximum principal axis of inertia aligned with the epithermal neutron palaeopole. The goal here is to find all possible I_{MA} that satisfy this condition.

The present-day lunar inertia tensor I can be determined directly from a combination of degree-2 spherical harmonic gravity coefficients, J_2 ($-C_{20}$) and C_{22}, and libration parameters, β and γ, and is well constrained[21,57,72,73]. In a principal-axis reference frame, the lunar inertia tensor can be written

$$I = \begin{bmatrix} A & 0 & 0 \\ 0 & B & 0 \\ 0 & 0 & C \end{bmatrix}$$

in which A, B and C are the minimum, intermediate and maximum principal moments of inertia. Following ref. 57, it is convenient to define these principal moments in terms of their departures from the mean moment of inertia

$$\frac{I}{MR^2} = \frac{A+B+C}{3MR^2} = \frac{2}{3}\left(-J_2 + \frac{6C_{22}}{\gamma}\right) = 0.39298$$

in which M and R are the mass and radius of the Moon, respectively. A, B and C can then be written

$$\frac{C-I}{MR^2} = \frac{2}{3}J_2 = 135.619 \times 10^{-6}$$
$$\frac{B-I}{MR^2} = -\frac{1}{3}J_2 + C_{22} = -23.019 \times 10^{-6}$$
$$\frac{A-I}{MR^2} = -\frac{1}{3}J_2 - 2C_{22} = 135.619 \times 10^{-6}$$

The inertia tensor of an arbitrary mass anomaly I_{MA} depends strongly on the assumed location, geometry and mass distribution of the perturbing mass anomaly. However, if we consider the limiting case of an axisymmetric anomaly centred on the north pole of the planet (such that the symmetry axis of the anomaly, and the z axis are aligned), then the inertia tensor of the anomaly is reduced to a single parameter. This is because an axisymmetric anomaly centred on the north pole will

contribute only to J_2, no other degree-2 spherical harmonic gravity coefficients, owing to symmetry. Following ref. 50, we then relate the degree-2 gravity of the mass anomaly located on the pole directly to an inertia tensor

$$I_{MA}^* = MR^2 \begin{bmatrix} \dfrac{I}{MR^2} - \dfrac{1}{3}J_2^{MA} & 0 & 0 \\ 0 & \dfrac{I}{MR^2} - \dfrac{1}{3}J_2^{MA} & 0 \\ 0 & 0 & \dfrac{I}{MR^2} + \dfrac{2}{3}J_2^{MA} \end{bmatrix}$$

in which J_2^{MA} is the degree-2 zonal spherical harmonic coefficient associated with the mass anomaly when centred on the north pole (aligned with the positive z axis). Because we are concerned only with the orientation of the principal axes of inertia (the maximum of which is presumed to be associated with a palaeopole), the mean moment of inertia can be neglected. The mean moment of inertia is spherically symmetric and does not control the orientation of the principal axis of inertia. (Stated another way: the mean moment of inertia affects the eigenvalues of the inertia tensor, but not the eigenvectors.) I_{MA}^* is the inertia tensor for the case in which the mass anomaly is located on the north pole (with the symmetry axis aligned with the positive z axis). To determine the inertia tensor for a mass anomaly located anywhere on the Moon, we rotate the inertia tensor: $I_{MA} = \mathcal{R}I_{MA}^*\mathcal{R}^\top$, in which $\mathcal{R}$ is a rotation matrix to rotate the mass anomaly from the north pole to an arbitrary latitude and longitude and $\mathcal{R}^\top$ is the transpose of $\mathcal{R}$. Ultimately, I_{MA} is simply a function of J_2^{MA} and the position (latitude and longitude) of the anomaly. For simplicity, we define the quantity $Q = -J_2^{MA}/J_2$, with J_2 the degree-2 zonal gravity harmonic measured by GRAIL[74]: $J_2 = -C_{20} = 203.2133 \times 10^{-6}$, in unnormalized spherical harmonic coefficients. The negative sign forces Q to be positive for positive mass anomalies and negative for negative mass anomalies.

To determine the possible locations and magnitudes of perturbing mass anomalies that could be responsible for the observed epithermal neutron palaeopole, we performed a parameter-space survey investigating the effect of placing mass anomalies of various sizes (Q) across the surface of the Moon. For each test case, we determined the palaeo inertia tensor: $I - I_{MA} = I_{palaeo}$.

We determined the orientations of the principal axes of inertia by evaluating the eigenvalues and eigenvectors of I_{palaeo}. We then measured the mean angular separation between the maximum principal axis of inertia and the epithermal neutron north and south poles. Extended Data Figure 7a–d shows example slices of this parameter-space search for positive and negative mass anomalies. The regions that can drive the required reorientation to within the measured uncertainty (approximately 1°) are limited. Figure 3a–c and Extended Data Fig. 7e show the acceptable regions in which a mass anomaly of a range of sizes (Q) could produce the required reorientation to within 1°.

Simple physical models for producing the required reorientation. Lunar impact basins, uncompensated topography and mare basalts can have a substantial contribution to the inertia tensor of the Moon[21,58,75]. To determine if these features were possibly responsible for the reorientation that is required to explain the epithermal neutron palaeopoles, we considered a simple case of a spherical cap of uniform surface density (Extended Data Fig. 8a). Extended Data Figure 8b shows Q for spherical caps as a function of surface density (which, assuming a material density, can be converted into an equivalent, uncompensated material thickness) and cap radius. For the typical sizes of large impact basins (radii of <15°), required mass anomalies (Fig. 3a–c; $|Q| > 0.2$) would be equivalent to >5 km of uncompensated topography (either a topographic excess or depression, depending on the sign of the surface density). This magnitude of uncompensated topography or mare basalts is not observed in any lunar impact basin. In the following section, we exclude impact basins and mare basalts in a more rigorous manner.

Internal mass anomalies, including mantle plumes or lateral variations in composition or density, can also have a contribution to the Moon's inertia tensor. For simplicity, we considered a simple spherical mass anomaly, spanning from the outer core to the lunar crust, with an arbitrary density contrast (Extended Data Fig. 8c). In this case, Q for this simple internal anomaly is dependent only on the density contrast, as shown in Extended Data Fig. 8d. The smallest required mass anomalies (Fig. 3a–c; $|Q| \approx 0.2$) would be equivalent to density anomalies of only $|\Delta\rho| \approx 10\,kg\,m^{-3}$. If these density anomalies are thought to arise from temperature variations, this would be equivalent to $|\Delta T| \approx 100\,K$ (assuming a 3,300 $kg\,m^{-3}$ mantle density and a volumetric coefficient of thermal expansion of 3×10^{-5})[76]. Temperature anomalies of this magnitude are easily generated in thermal evolution models of the PKT[8-11]. This drives our detailed investigation of the TPW potential of the PKT.

The contribution of impact basins to the lunar inertia tensor. To determine whether impact-basin features can produce the mass anomalies required to explain

the epithermal neutron palaeopole, we used the method of ref. 21 to isolate the degree-2 gravity field of these features. Extended Data Figure 8f shows the best-fit mass anomaly (Q) associated with each of the 32 largest lunar impact basins.

From Extended Data Fig. 8f it is clear that most lunar impact basins have a small contribution to the degree-2 gravity field of the Moon—with the exception of the South Pole–Aitken basin, and its associated ejecta blanket. All other impact basins have $|Q| < 0.2$, which is the smallest possible value of Q that can reorient the Moon enough to explain the epithermal neutron palaeopoles (Fig. 3a–c). The only large impact basin that is located in a place that could potentially reorient the Moon in the necessary direction is Moscoviense (27° N, 148° E). For it to cause the observed reorientation, Moscoviense would need to be a present-day positive mass anomaly, with $Q \approx +0.22$ (Fig. 3a–c). From the inverse modelling of this basin's gravity field, we find that Moscoviense is a net negative mass anomaly, with $Q < 0.1$. Thus, even the favourably located Moscoviense impact basin is not capable of causing the required reorientation.

Lunar impact basins tend to have a negligible contribution to degree-2, owing to the detailed structure of their gravity fields. Large lunar impact basins frequently possess large, central, positive free-air anomalies (so-called 'mascons'[77]), surrounded by a broad, negative free-air anomaly collar resulting from the deposition of ejecta and thickening of the crust[78]. This alternating positive/negative 'bull's-eye' pattern results in an almost net-zero contribution to the degree-2 gravity field[21]. It is possible that impact basins had more substantial contributions to degree-2 shortly after they formed, and before the formation of the central mascon, due to viscoelastic relaxation, mantle-flow, and cooling and contraction of the impact melt pool; however, this would be a transient stage lasting less than 30 Myr (ref. 78). It is unlikely that all of the observed hydrogen deposits formed in such a short time-span. Furthermore, if large impact basins were responsible, then we would expect several sets of antipodal epithermal neutron deposits, rather than just one.

Although the South Pole–Aitken basin and its associated global ejecta blanket easily produce mass anomalies comparable to those required to explain the epithermal neutron palaeopoles[21] (Extended Data Fig. 8f), it is not at the proper location to reorient the Moon in the necessary direction (Fig. 3b). In fact, the location of the South Pole–Aitken basin is incompatible with the observed epithermal neutron palaeopole. Extended Data Figure 8e illustrates the range of possible palaeopoles for both the South Pole–Aitken basin and the PKT, for a wide range of mass anomalies centred on each feature (the entire parameter space of Extended Data Fig. 8b). The latitude and longitude of the perturbing mass anomaly immediately restricts the possible locations for a palaeopole. The set of possible palaeopoles for PKT naturally passes through the epithermal neutron palaeopoles, whereas the possible palaeopoles associated with the South Pole–Aitken basin are nearly orthogonal to the observed reorientation. Thus, the South Pole–Aitken basin cannot be responsible for the observed epithermal neutron palaeopoles (although asymmetries in the impact basin and associated ejecta blanket[79] may complicate this picture).

Evolution of the lunar inertia tensor due to the formation and evolution of the PKT. To determine the reorientation of the Moon due to the thermal evolution of the Procellarum KREEP Terrain (PKT), we used the 3D thermochemical convection models of ref. 9 (see ref. 9 for the details of the model). Here, we focus on how we use these models to determine the TPW history of the Moon.

The PKT thermal models consist of a 3D spherical grid, with 20-km radial resolution and 60-km lateral resolution. The radial grid runs from the core–mantle boundary (at a radius of $R_C = 390$ km) to the Moon's surface ($R_P = 1,740$ km). At each volume element within the model domain, the density varies owing to thermal expansion/contraction; in the bulk composition, it varies owing to partial melting and subsequent melt migration. We determine the full inertia tensor of the model by summing the contribution of each volume element

$$I_{xx} = \sum_i \rho_i V_i (y_i^2 + z_i^2)$$
$$I_{xy} = -\sum_i \rho_i V_i x_i y_i$$

and similarly for the other components of the inertia tensor ($I_{yy}, I_{zz}, I_{xz}, I_{yz}$). Here, V_i is the volume of the ith grid element and ρ_i is the density, which varies with time. In these calculations, we take PKT to be located along the positive z axis.

For TPW, it is not only important to consider density variations within the body, but also surface deformation in response to the temperature evolution at depth. As the mantle heats up, the surface will be uplifted in response to the thermal expansion of the mantle. Depending on the magnitude of this surface compensation, it is possible for PKT to act as either a net negative anomaly ($Q < 0$; if the thermal anomaly at depth dominates) or a net positive anomaly ($Q > 0$; if the topographic uplift dominates). Our PKT models do not directly take into account changes in surface topography due to thermal evolution at depth. To address this, we followed the

approach used in ref. 9 and calculated the amount of surface uplift *a posteriori* by determining the amount of topography necessary to balance the thermal expansion/contraction of the mantle at depth. For each radial column within the model domain, we determined the initial integrated mass within that column. As the interior warms owing to the evolution of PKT, this results in an overall decrease in density in the column, which in an incompressible model without surface flexure, leads to a small decrease in the integrated mass within the column. If we assume that the lithosphere can perfectly compensate for this change in density (which would occur only if the lithosphere was completely strengthless), then we add this missing mass back into the model at the uppermost radial volume element within the column. This added mass is a proxy for the topographic uplift resulting from this interior changes in density. Because real planetary lithospheres are not strengthless, and instead possess some rigidity, we modulated this correction by a factor we term the 'compensation state' C. If $C = 1$, then we add in the complete mass correction corresponding to a strengthless lithosphere. If $C = 0$, then we do not add in any mass correction, which would correspond to a completely rigid lithosphere, incapable of deforming in response to the interior thermal expansion. Thus, the total inertia tensor I_{PKT} from the thermal model is $I_{PKT} = I_{interior} + C I_{topography}$, in which $I_{interior}$ is the inertia tensor that results from summing up the contribution of each volume element within the model and $I_{topography}$ is the inertia tensor that results from the mass due to this dynamic topography in the upper-most grid cell. For all cases, we normalize the final total inertia tensor to the observed mass and radius of the Moon.

From the inertia tensor, it is possible to directly calculate spherical harmonic gravity coefficients[50]

$$C_{20} = -J_2 = -\frac{I_{zz} - \frac{1}{2}(I_{xx} + I_{yy})}{MR^2}$$
$$C_{21} = -\frac{I_{xz}}{MR^2}$$
$$C_{22} = -\frac{\frac{1}{4}(I_{xx} - I_{yy})}{MR^2}$$
$$S_{21} = -\frac{I_{yz}}{MR^2}$$
$$S_{22} = -\frac{\frac{1}{2}I_{xy}}{MR^2}$$

For the case with the PKT centred on the z axis, the degree-2 gravity field associated with PKT is described primarily by C_{20}, owing to symmetry. Although there is some power in the other spherical harmonic gravity coefficients, C_{20} is the most important. The inertia tensor is uniquely related to degree-2 gravity coefficients (and only degree-2 gravity coefficients).

In our parameter-space search for possible perturbing mass anomalies (Fig. 3a–c), we assume that the Moon used to have its spin axis at a different location (possibly at the epithermal neutron palaeopole) and was subsequently reoriented to the present-day spin pole. Phrased differently, we assume that the perturbing mass anomaly is still present, and still contributes to the observed lunar inertia tensor and degree-2 spherical harmonic gravity coefficients. Thus, to determine the relative importance of the PKT, it is more useful to define the change in the mass-anomaly size with respect to its present value: $\Delta Q = Q(t) \Delta Q(0 \text{ Gyr ago})$. This ΔQ is the relevant quantity for the parameter-space survey in Fig. 3a–c, and determines how much the Moon could have reoriented in the past, with respect to its present-day orientation. A positive ΔQ indicates the presence of a positive mass anomaly (mass excess) with respect to the present state; a negative ΔQ indicates the presence of a negative mass anomaly (mass deficit) with respect to the present state. Q and ΔQ for two end-member PKT thermal anomalies are shown in Extended Data Figs 9, 10. The nomenclature 'W' and 'B' are shortened from '0LW' and '0LB' adopted from ref. 9, in which '0' denotes low radiogenic mantle composition and 'L' denotes the larger (in diameter) of two test cases, 'W' denotes KREEP within the crust and 'B' denotes KREEP below the crust.

True polar wander due to the PKT. To determine how the Moon would reorient under the thermal evolution of the PKT, it is necessary to first reorient the PKT inertia tensor so that it is properly aligned with the approximate centre of the PKT (18° N, 334° E). This can be done by either directly rotating the inertia tensor or rotating the spherical harmonic gravity coefficients via the spherical harmonic addition theorem[57,80].

To determine the TPW path predicted from the thermal evolution of the PKT, it is necessary to determine the location of the maximum axis of inertia as a function of time. The location of this maximum axis of inertia is defined as the palaeopole. To calculate this TPW path for any PKT thermal model, we first assume that the

present-day, observed lunar inertia tensor is the sum of the inertia tensor from the final time-step of the thermal evolution models ($t = 0$ Gyr ago), and some non-hydrostatic component (including other impact basins, mascons the fossil figure and so on) I_{NH}: $I = I_{PKT}(0\,\text{Gyr ago}) + I_{NH}$. In this calculation, we remove the hydrostatic component of the present-day, observed lunar inertia tensor[73]. Although much of the geologic history outside of the PKT is buried within I_{NH}, it is important to note that most of the other geologic processes on the Moon (for example, impact basins and mare basalts) have negligible contributions to the lunar inertia tensor[21] (Extended Data Fig. 8f). The most substantial other contributors are the South Pole–Aitken basin and its global ejecta blanket[21], and the Moon's fossil figure—the remnant rotational and tidal bulge, preserved from when the Moon's lithosphere cooled sufficiently to support long-term deformation. Although the nature of the fossil figure is debated[20,21], and the formation of the South Pole–Aitken basin is still poorly understood[79], both of these events would have occurred very early in lunar history, probably predating the initial conditions of our PKT thermal model. Thus, we do not expect I_{NH} to change appreciably during the course of lunar history, but rather expect only negligible perturbations due to the formation of impact basins with time. Because I is known and $I_{PKT}(0\,\text{Gyr ago})$ is inferred from our PKT thermal evolution models, we rearrange the above equation ($I = I_{PKT}(0\,\text{Gyr ago}) + I_{NH}$) to determine I_{NH}.

By isolating the non-PKT, non-hydrostatic component of the lunar inertia tensor, we then determine the inertia tensor as a function of time from our PKT thermal models: $I(t) = I_{PKT}(t) + I_{NH}$. The palaeopole can be calculated at any time-step in the model by taking the inertia tensor at that time, evaluating the eigenvalue problem and identifying the orientation of the maximum axis of inertia. Figure 4 and Extended Data Figs 9 and 10 show representative TPW tracks calculated using this method. Supplementary Video 1 shows an example of this TPW for our nominal model (model W; $C = 0$), as viewed from an outside observer. As a consequence of our definition of I_{NH}, the TPW track will always end at the present-day rotation pole. However, the TPW track is not forced to pass through the epithermal neutron palaeopole, although this happens frequently, owing to the placement of the PKT model at the PKT.

The thermal evolution of the PKT is not completely axisymmetric about the centre of the PKT, owing to the 3D nature of the problem. This results in intermediate and minimum principal axes of inertia that are not quite equal ($I_{xx} \neq I_{yy}$), in addition to small, non-zero off-diagonal terms in the inertia tensor ($I_{xy} \neq I_{xz} \neq I_{yz} \neq 0$). These terms can have a small effect on the orientation of the maximum principal axis of inertia derived using the above method. To account for this variation, we rotate the PKT anomaly about the vector aligned with the PKT, and repeat the analysis for all possible PKT rotation angles. Error bars in our TPW paths (for example, in Fig. 4) indicate the 1σ uncertainty in the palaeopole position that results from this effect. In general, it is negligible.

Thus far, we have only considered solutions where the compensation state of the lunar crust is constant with time and independent of the position on the surface of the Moon. More complicated histories of the strength of the lithosphere might be possible, but a full parameter-space survey is beyond the scope of this work. In Extended Data Fig. 10m–o, we present three example TPW tracks for cases for which the compensation state varies monotonically with time.

Models that allow for the compensation state to increase with time (Extended Data Fig. 10n, o) produce TPW tracks that would markedly reduce the age of the epithermal neutron palaeopole (to only about 1.5 Gyr in Extended Data Fig. 10o). Although this sort of weakening of the lithosphere with time might not be physical, it is possible that the loading and isostatic adjustment (or non-adjustment) of the PKT mare basalts and other near-surface mass anomalies could replicate the effect of this time-varying compensation state. Thus, further study of the geologic and geophysical history of the PKT could provide insight into the long-term stability of lunar polar ice.

Plausible modes of long-term hydrogen stability. Our nominal TPW models suggest a source for the observed off-polar hydrogen (plausibly in the form of water ice) that predates the migration of the lunar spin axis. Because this hydrogen would have to survive for what could amount to several billion years, it may have experienced temperature conditions warmer than present. Therefore, it is important to consider the long-term stability of polar hydrogen.

Water ice will be stable if the temperatures in first few metres of the Moon's surface remain below about 145 K. Even near the poles, directly illuminated surfaces will experience maximum temperatures that exceed 145 K, which leads to ground ice being stable only within polar craters or regions with high topographic relief[5]. Above this temperature, water ice (thicker than a single surface-bound monolayer) will sublime on geologic timescales, with rates exceeding $1\,\text{mm}\,\text{Gyr}^{-1}$ (refs 25, 81).

Although a single monolayer of water is more stable, it is probably not sufficient to cause the observed hydrogen excess. A typical sample of Apollo lunar regolith has a surface area of about $0.5\,\text{m}^2\,\text{g}^{-1}$ (refs 82, 83). An idealized monolayer

contains approximately 10^{15} molecules per square centimetre, so a monolayer contains approximately 5×10^{18} molecules per gram of regolith. This corresponds to a mass of 1.5×10^{-4} grams of H_2O, or 17 p.p.m. of hydrogen atoms. Although variations in grain size may change the ratio of surface area to volume (and thus the mass fraction of hydrogen), with these assumptions, adsorption of water molecules directly to regolith can contribute only a small fraction of the minimum plausible hydrogen concentration observed at the epithermal neutron palaeopole (Fig. 1a, b). Thus, we assume that the observed hydrogen corresponds to either water ice mixed within regolith (pore ice), or hydrogen bound within mineral grains.

Ancient ice must also survive billions of years of impact gardening, a process that will slowly mix ice with the surrounding regolith[13,84]. Impact gardening can result in both ice loss, because ice is brought to the warmer near-surface, and preservation of ice, because ice is buried under layers of protective, thermally insulating regolith. However, impact gardening processes will dominate only if the water ice is completely immobile (as would be the case for adsorbed water). Given even short window of time with temperatures above about 70–90 K, buried water molecules can migrate towards the surface, driven solely by the water vapour concentration gradient between the regolith and the vacuum of space. Water will migrate upward until it hits the predicted ice stability depths (Fig. 1c, d, Extended Data Fig. 4) where it will remain and concentrate, because loss rates to space are slow enough ($1\,\text{mm}\,\text{Gyr}^{-1}$) that it will not thermally sublimate over geologic time. The ice may be buried again, mixed into the regolith or lost by an impact related process, but, assuming some small amount of thermal mobility, it will again return to the ice stability depth. Therefore, even accounting for impact gardening, as long as temperatures remain greater than about 70–90 K, but never exceed about 145 K, the predicted depths should be a good proxy for detectable hydrogen.

Ice stability models presented here show that ice can be stable both at the current and proposed palaeopole orientations. Extended Data Figure 4e, f shows that there are large areas that are stable in the upper 2.5 m for ice both at the current lunar pole position and at the proposed palaeopole (ice stability depth is assigned as an average of the two models). However, if wander led to a spin pole much further from the palaeopole, ground ice would no longer be stable in these locations. To estimate how far a shadowed crater could move from the pole and still retain large amounts of ground ice, we look at previous studies examining the effects of lunar obliquity on ice stability. In such studies, a polar crater (Shackleton) was found to retain stable ice until the Moon tilted by $>12°$ (refs 4, 49). We use this 12° limit as an approximate estimate for the maximum extent of polar wander that can occur with respect to a palaeopole and still allow for the preservation of water ice at the pole. In fact, some wander past the current pole would aid in the migration of buried water to the surface by creating slightly warmer conditions than present. At present, some cold traps are so cold (maximum temperatures $< 90\,\text{K}$) that ice is effectively immobile[25], leaving it to be slowly buried by impact gardening[13]. TPW might have caused these areas to experience conditions warm enough that ice buried by impact gardening would migrate towards the surface ($\sim 90\,\text{K} < T < 145\,\text{K}$), driven by the concentration gradient (with the vacuum of space).

Although many of our TPW paths remain within this 12° ice-stability limit, suggesting that the hydrogen observed at the epithermal neutron palaeopole is plausibly water ice (Fig. 4a, b, Extended Data Fig. 10a–d, n, o), many do not. In these 'large wander' cases, the shadowed regions near the epithermal palaeopole may have experienced temperatures that exceeded the 145-K stability limit for water ice. This would suggest that the epithermal neutrons may be mineralogically trapped or bound hydrogen, rather than pore ice. Most mineralogies will have higher bonding strength than that of water to water, and be more stable to large temperature fluctuations. It may be that pore ice was originally stable at these locations, but has since been partially lost (perhaps via hydrothermally interacting with the surrounding regolith), leaving only the most stable forms of hydrogen behind. However, impact gardening will slowly bury the grains this water is bound to and thus limit the length of time such hydrogen will be in sufficient abundances to be detectable via neutron spectrometry.

It is also plausible that the observed hydrogen might never have been water. Hydrogen can implant into permanently shadowed regions both from Earth's magnetotail and by backscattering of solar-wind hydrogen off of nearby irradiated crater walls. However, an explanation of why such a mechanism would result in the observed antipodal ice distribution has not been proposed. Perhaps areas that once harboured water ice are more accepting of solar-wind hydrogen. The time required to build up about 100 p.p.m. of rim-entrapped hydrogen in a permanently shadowed region has been estimated[28] to be of the order of 200 Myr. If not continuously resupplied, then hydrogen trapped at defects in grain rims has a chance to escape, with this chance depending primarily on two variables: diffusion activation energy and temperature. A range of realistic activation energies were found[85] for which hydrogen would be retained at low lunar temperatures and for billions of years.

Regardless of the hydrogen source, defects in weathered grain rims can create a large volume for hydrogen retention, and may be sufficient to explain the observed hydrogen concentrations. The possible retention of hydrogen trapped at defects within the rims of the lunar grains themselves has been calculated[28,86]. The maximum concentration is set by the maximum retention of implanted hydrogen in laboratory experiments, and is about 2×10^{17} cm^{-2}. The thickness of the implantation rim is taken to be 100 nm. For a lunar soil surface area of 0.5 m^{2}g^{-1}, the maximum trapped-hydrogen concentration is about 1.700 p.p.m. (ref. 28).

Large-scale defects, such as radiation tracks, can react with water[87–91]. Such a situation could occur as once-stable ice deposits begin to sublimate. This reaction was shown to increase the specific surface area and porosity of lunar fines and retain water. However, it is unclear how long might water stay within the grain lattice once it is established there. We adopt a silicate lattice of 3.3 g cm^{-3} and, hence, an atomic density of about 10^{23} cm^{-3}; we assume a water density of about 10^{20} cm^{-3}. By using Fick's law[92], with a typical silicate diffusion coefficient of $D = 10^{-25}$ cm^2 s^{-1}, and calculating the flux J across a 1-μm lattice layer into the vacuum (so that 10^{20} cm^{-3} drops to 0 cm^{-3} in 10^{-4} cm), we obtain

$$J = D\frac{\partial n}{\partial x} = 10^{-25}\, \text{cm s}^{-1} \times \frac{10^{20}\, \text{cm}^{-3}}{10^{-4}\, \text{cm}} = 0.1\, \text{cm}^{-2}\, \text{s}^{-1}$$

The number of water molecules in a 1 μm × 1 cm^2 volume is 10^{16}, so the diffusion timescale is $10^{16}/(0.1\, \text{s}^{-1}) = 10^{17}$ s = 3 Gyr. Using values from the literature[93,94], we estimate $D \approx 10^{-28}$ and $J \approx 10^{-4}$ cm^{-2} s^{-1}, which implies that water, having incorporated into lunar materials, will not diffuse from the outer micrometres in several billion years.

The mechanisms described above may allow for reasonable long-term (Gyr) storage of hydrogen—either in the form of pore ice or mineralogically bound hydrogen—in the off-polar regions detected by the epithermal neutron data presented here. However, the evidence presented here points to a correlation with preferential water stability along the path of TPW.

It is possible that the epithermal neutron distribution marks the surviving hydrogen from an epoch of ice stability or high supply (for example, the late heavy bombardment, a time during which the Moon had a protective magnetic field, or primordial internal water from the Moon's formation); alternatively, it could trace a history of later-stage addition of hydrogen (for example, outgassing of water from mare volcanism, large volatile-rich impacts or some variation in solar wind). Future orbital missions with high-resolution, high-precision neutron spectrometers might be able to better constrain the extent of the polar hydrogen, and future *in situ* polar landers or sample return might be able to directly determine the nature of lunar polar hydrogen. Current evidence, such as the detection of water ice in the LCROSS-impact vapour plume[26] (this impact occurred very close to our proposed southern palaeopole), suggests that the observed hydrogen enhancement is due to water, and that the Moon may not have wandered an extreme amount since the deposition of this water.

31. Mitrofanov, I. G. *et al.* Experiment LEND of the NASA Lunar Reconnaissance Orbiter for high-resolution mapping of neutron emission of the Moon. *Astrobiology* **8,** 793–804 (2008).
32. Litvak, M. L. *et al.* Global maps of lunar neutron fluxes from the LEND instrument. *J. Geophys. Res. Planets* **117,** E00H22 (2012).
33. Lawrence, D. J., Elphic, R. C., Feldman, W. C., Funsten, H. O. & Prettyman, T. H. Performance of orbital neutron instruments for spatially resolved hydrogen measurements of airless planetary bodies. *Astrobiology* **10,** 183–200 (2010).
34. Lawrence, D. J. *et al.* Technical Comment on "Hydrogen mapping of the lunar south pole using the LRO neutron detector experiment LEND". *Science* **334,** 1058 (2011).
35. Eke, V. R., Teodoro, L. F. A., Lawrence, D. J., Elphic, R. C. & Feldman, W. C. A quantitative comparison of lunar orbital neutron data. *Astrophys. J.* **747,** 6 (2012).
36. Teodoro, L. F. A., Eke, V. R., Elphic, R. C., Feldman, W. C. & Lawrence, D. J. How well do we know the polar hydrogen distribution on the Moon? *J. Geophys. Res. Planets* **119,** 574–593 (2014).
37. Feldman, W. C. *et al.* Gamma-ray, neutron, and alpha-particle spectrometers for the Lunar Prospector mission. *J. Geophys. Res. Planets* **109,** E07S06 (2004).
38. Maurice, S., Lawrence, D. J., Feldman, W. C., Elphic, R. C. & Gasnault, O. Reduction of neutron data from Lunar Prospector. *J. Geophys. Res. Planets* **109,** E07S04 (2004).
39. Lawrence, D. J. *et al.* Improved modeling of Lunar Prospector neutron spectrometer data: implications for hydrogen deposits at the lunar poles. *J. Geophys. Res.* **111,** E08001 (2006).
40. Press, W.H., Teukolsky, S.A., Vetterling, W.T. & Flannery, B. P. *Numerical Recipes in C: The Art of Scientific Computing* Ch. 14.5, 636–639 (1992).
41. Fisher, R. A. Frequency distribution of the values of the correlation coefficient in samples from an infinitely large population. *Biometrika* **10,** 507–521 (1915).
42. Watson, K., Murray, B. & Brown, H. On the possible presence of ice on the Moon. *J. Geophys. Res.* **66,** 1598–1600 (1961).
43. Harmon, J. K., Slade, M. A. & Rice, M. S. Radar imagery of Mercury's putative polar ice: 1999–2005 Arecibo results. *Icarus* **211,** 37–50 (2011).
44. Chabot, N. L. *et al.* Areas of permanent shadow in Mercury's south polar region ascertained by MESSENGER orbital imaging. *Geophys. Res. Lett.* **39,** L09204 (2012).
45. Lawrence, D. J. *et al.* Evidence for water ice near Mercury's north pole from MESSENGER neutron spectrometer measurements. *Science* **339,** 292–296 (2013).
46. Lawrence, D. J., Miller, R. S., Ozimek, M. T., Peplowski, P. N. & Scott, C. J. High-resolution mapping of lunar polar hydrogen with a low-resource orbital mission. *Acta Astronaut.* **115,** 452–462 (2015).
47. Tye, A. R. *et al.* The age of lunar south circumpolar craters Haworth, Shoemaker, Faustini, and Shackleton: implications for regional geology, surface processes, and volatile sequestration. *Icarus* **255,** 70–77 (2015).
48. Ward, W. R. Past orientation of the lunar spin axis. *Science* **189,** 377–379 (1975).
49. Siegler, M. A., Bills, B. G. & Paige, D. A. Effects of orbital evolution on lunar ice stability. *J. Geophys. Res. Planets* **116,** E03010 (2011).
50. Lambeck, K. *The Earth's Variable Rotation: Geophysical Causes and Consequences* (Cambridge Univ. Press, 1980).
51. Sabadini, R. & Vermeersen, B. *Global Dynamics of the Earth: Applications of Normal Mode Relaxation Theory to Solid-Earth Geophysics* (Kluwer, 2004).
52. Van Hoolst, T. in *Treatise on Geophysics: Planets and Moons* (eds Schubert, G. & Spohn, T.) 123–164 (Elsevier, 2009).
53. Colombo, G. in *Measure of the Moon* (eds Kopal, Z. & Goudas, C. L.) 12–22 (Springer, 1967).
54. Peale, S. J. Generalized Cassini's laws. *Astron. J.* **74,** 483–488 (1969).
55. Gold, T. Instability of the Earth's axis of rotation. *Nature* **175,** 526–529 (1955).
56. Goldreich, P. & Toomre, A. Some remarks on polar wandering. *J. Geophys. Res.* **74,** 2555–2567 (1969).
57. Matsuyama, I. Fossil figure contribution to the lunar figure. *Icarus* **222,** 411–414 (2013).
58. Melosh, H. J. Mascons and the Moon's orientation. *Earth Planet. Sci. Lett.* **25,** 322–326 (1975).
59. Runcorn, S. K. Lunar magnetism, polar displacements and primeval satellites in the Earth–Moon system. *Nature* **304,** 589–596 (1983).
60. Runcorn, S. K. The primeval axis of rotation of the Moon. *Phil. Trans. R. Soc. Lond. A* **313,** 77–83 (1984).
61. Hood, L. L. Central magnetic anomalies of Nectarian-aged lunar impact basins: probable evidence for an early core dynamo. *Icarus* **211,** 1109–1128 (2011).
62. Cournède, C., Gattacceca, J. & Rochette, P. Magnetic study of large Apollo samples: possible evidence for an ancient centered dipolar field on the Moon. *Earth Planet. Sci. Lett.* **331–332,** 31–42 (2012).
63. Tsunakawa, H., Takahashi, F., Shimizu, H., Shibuya, H. & Matsushima, M. Surface vector mapping of magnetic anomalies over the Moon using Kaguya and Lunar Prospector observations. *J. Geophys. Res. Planets* **120,** 1160–1185 (2015).
64. Kim, H. R., Hood, L. L., von Frese, R. R. B. & O'Reilly, B. E. Nectarian paleomagnetic pole inferred from Kaguya satellite magnetic observations of the central Leibnitz basin. *Lunar Planet. Sci. Conf.* **46,** 1914 (2015).
65. Iess, L. *et al.* The gravity field and interior structure of Enceladus. *Science* **344,** 78–80 (2014).
66. Matsuyama, I. & Nimmo, F. Tectonic patterns on reoriented and despun planetary bodies. *Icarus* **195,** 459–473 (2008).
67. Schenk, P., Matsuyama, I. & Nimmo, F. True polar wander on Europa from global-scale small-circle depressions. *Nature* **453,** 368–371 (2008).
68. Nimmo, F. & Manga, M. in *Europa* (eds Pappalardo, R. T. et al.) 381–404 (Univ. Arizona Press, 2009).
69. Perron, J. T., Mitrovica, J. X., Manga, M., Matsuyama, I. & Richards, M. A. Evidence for an ancient Martian ocean in the topography of deformed shorelines. *Nature* **447,** 840–843 (2007).
70. Kite, E. S., Matsuyama, I., Manga, M., Perron, J. T. & Mitrovica, J. X. True Polar Wander driven by late-stage volcanism and the distribution of paleopolar deposits on Mars. *Earth Planet. Sci. Lett.* **280,** 254–267 (2009).
71. Weiss, B. P. & Tikoo, S. M. The lunar dynamo. *Science* **346,** 1246753 (2014).
72. Bills, B. G. & Rubincam, D. P. Constraints on density models from radial moments: applications to Earth, Moon, and Mars. *J. Geophys. Res. Planets* **100,** 26305–26315 (1995).
73. Konopliv, A. S. *et al.* Improved gravity field of the Moon from Lunar Prospector. *Science* **281,** 1476–1480 (1998).
74. Zuber, M. T. *et al.* Gravity field of the Moon from the Gravity Recovery and Interior Laboratory (GRAIL) mission. *Science* **339,** 668–671 (2013).
75. Melosh, H. J. Large impact craters and the Moon's orientation. *Earth Planet. Sci. Lett.* **26,** 353–360 (1975).
76. Turcotte, D. L. & Schubert, G. *Geodynamics* 2nd edn, Ch. 4, 132–194 (Cambridge Univ. Press, 2002).
77. Muller, P. M. & Sjogren, W. L. Mascons: lunar mass concentrations. *Science* **161,** 680–684 (1968).
78. Melosh, H. J. *et al.* The origin of lunar mascon basins. *Science* **340,** 1552–1555 (2013).
79. Kendall, J. D., Johnson, B. C., Bowling, T. J. & Melosh, H. J. Ejecta from south pole-Aitken basin-forming impact: dominant source of farside lunar highlands. *Lunar Planet. Sci. Conf.* **46,** 2765 (2015).

80. Arfken, G. B. & Weber, H. J. *Mathematical Methods for Physicists* 4th edn, 797–798 (Academic Press, 1995).
81. Schorghofer, N. The lifetime of ice on main belt asteroids. *Astrophys. J.* **682,** 697–705 (2008).
82. Cadenhead, D. A., Wagner, N. J., Jones, B. R. & Stetter, J. R. Some surface characteristics and gas interactions of Apollo 14 fines and rock fragments. *Proc. Lunar Planet. Sci. Conf.* **3,** 2243–2257 (1972).
83. Heiken, G. H., Vaniman, D. T., French, B. M. (eds) *Lunar Sourcebook: A User's Guide to the Moon* Ch. 7, 285–356 (Cambridge Univ. Press, 1991).
84. Crider, D. & Killen, R. M. Burial rate of Mercury's polar volatile deposits. *Geophys. Res. Lett.* **32,** L12201 (2005).
85. Farrell, W. M., Hurley, D. M. & Zimmerman, M. I. Solar wind implantation into lunar regolith: hydrogen retention in a surface with defects. *Icarus* **255,** 116–126 (2015).
86. Starukhina, L. V. Polar regions of the moon as a potential repository of solar-wind-implanted gases. *Adv. Space Res.* **37,** 50–58 (2006).
87. Fuller, E. L. Jr. Interaction of gases with lunar materials (12001): textural changes induced by sorbed water. *J. Colloid Interface Sci.* **55,** 358–369 (1976).
88. Gammage, R. B. & Holmes, H. F. Blocking of the water-lunar fines reaction by air and water concentration effects. *Proc. Lunar Sci. Conf.* **6,** 3305–3316 (1975).
89. Gammage, R. B. & Holmes, H. F. Alteration of Apollo 17 orange fines by adsorbed water vapor. *J. Colloid Interface Sci.* **55,** 243–251 (1976).
90. Gammage, R. B. & Holmes, H. F. Effect of annealing temperature on the reactivity of lunar fines toward adsorbed water. *Earth Planet. Sci. Lett.* **34,** 445–449 (1977).
91. Holmes, H. F. *et al.* Alteration of an annealed and irradiated lunar fines sample by adsorbed water. *Earth Planet. Sci. Lett.* **28,** 33–36 (1975).
92. Fick, A. V. On liquid diffusion. *Phil. Mag.* **10,** 30–39 (1855).
93. Brady, J. B. in *Mineral Physics & Crystallography: A Handbook of Physical Constants* (ed. Ahrens, T. J.) 269–290 (American Geophysical Union, 1995).
94. Zhang, Y. Diffusion in minerals and melts: theoretical background. *Rev. Mineral. Geochem.* **72,** 5–59 (2010).
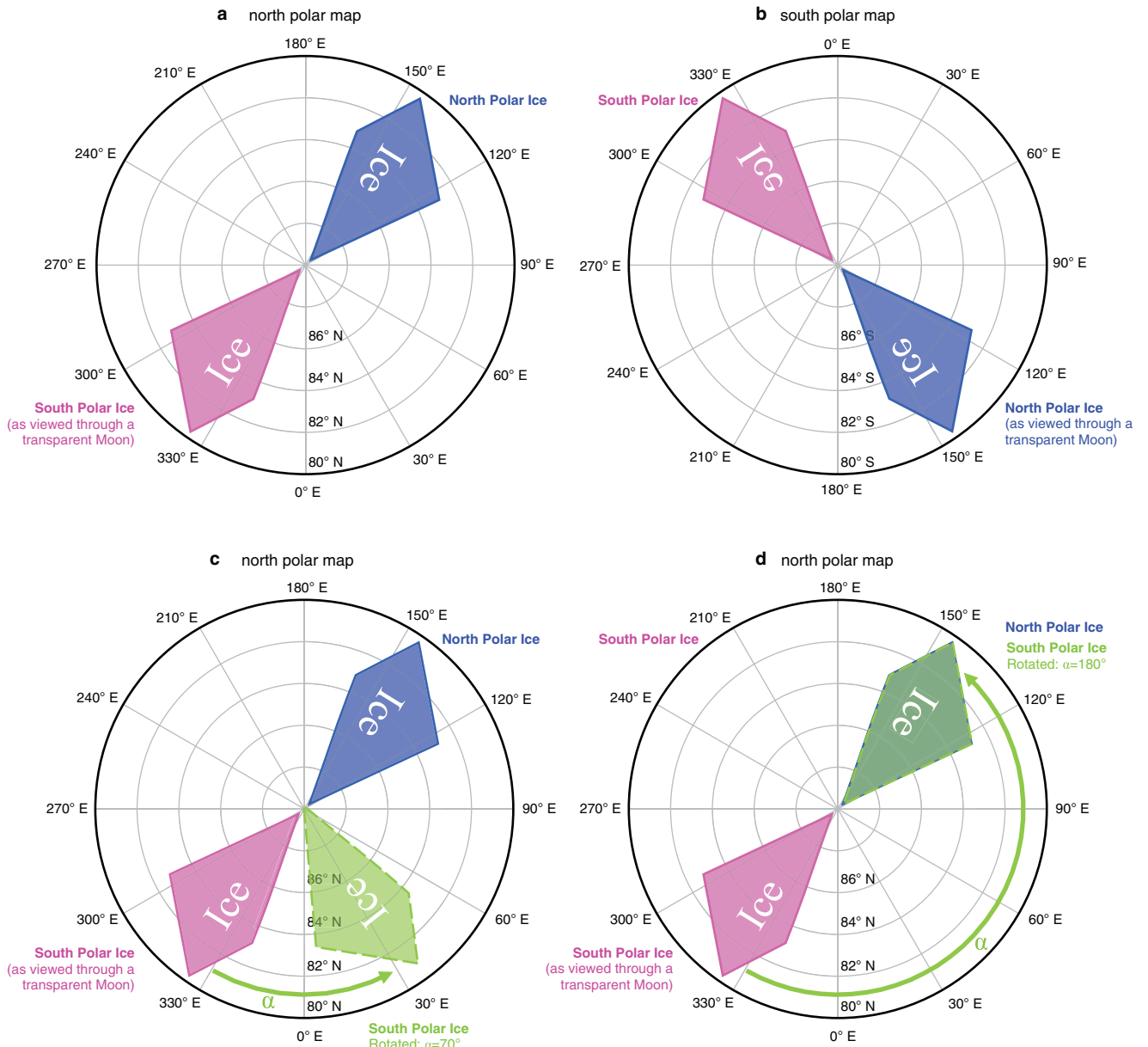
Extended Data Figure 1 | Antipodal symmetry. a, **b**, Standard north and south polar maps, respectively, akin to Fig. 1a, b. In each figure we show a hypothetical distribution of antipodally symmetric north (blue) and south (pink) polar ice. In each polar map, we show both the ice present in that hemisphere and the ice on the opposite hemisphere as it would be viewed through the Moon. Despite the antipodal symmetry, the polar ice that would be normally shown in each polar map (blue in **a**; pink in **b**) are not separated by 180° as one might expect. **c**, To test for antipodal symmetry, we rotate the features as viewed through the planet by an angle α. **d**, Antipodally symmetric features match their antipodal counterparts if rotated by $\alpha = 180°$.
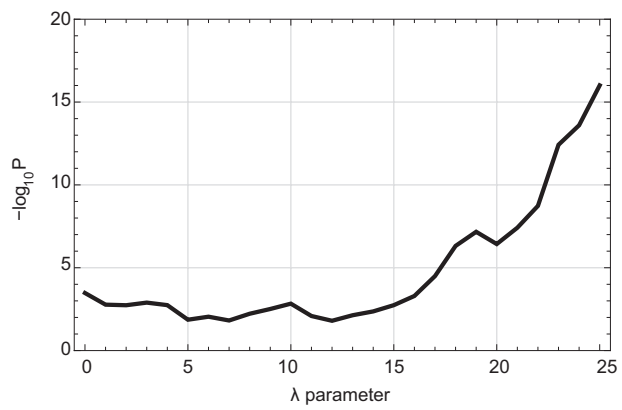
Extended Data Figure 2 | Statistical significance of inter-polar hydrogen. The statistical significant $-\log_{10}(P)$ is shown as a function of the likelihood parameter λ.
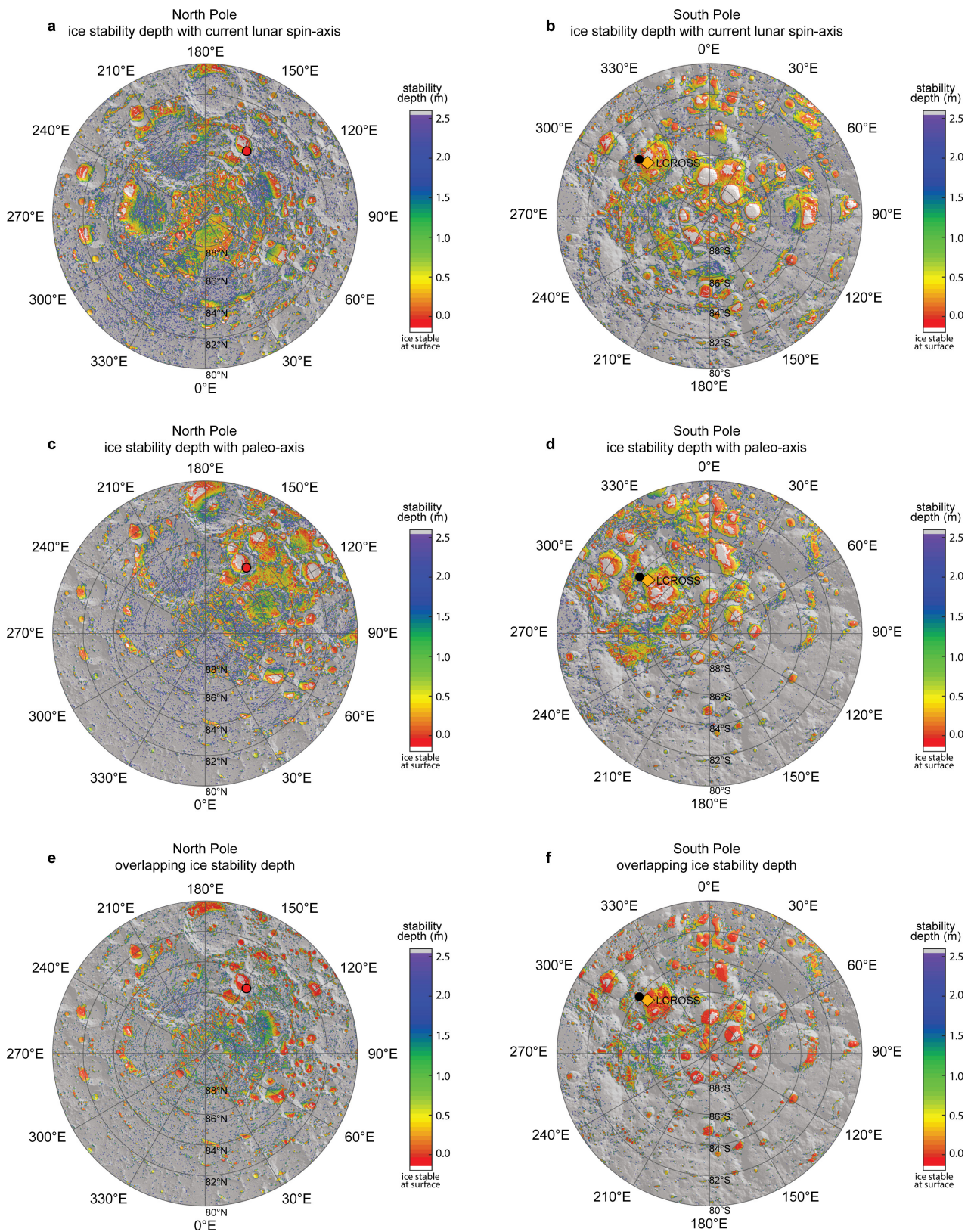
Extended Data Figure 3 | Full-resolution maps of ice stability depth.
The ice stability depth is defined as the depth at which water ice will sublimate at a rate of 1 mm Gyr^{-1}). **a–f**, Full-resolution maps of ice stability depth for areas where water ice is stable at the current orientation (**a**, **b**), in the palaeopole orientation (**c**, **d**) and in an 'overlapping' orientation (**e**, **f**); left panels shown the north polar region, right panels show the south. These models define the locations at which isotropically supplied water ice would be stable over geologic time; depth is given as an average of the two models in those locations. Panels **a–d** are the bases for Fig. 1c, d. Models are constrained to ± 300 km in stereographic x, y coordinates. Latitude lines are every 2° poleward of 80°. All other symbols are defined in Fig. 1. Panel **b** adapted from ref. 5, American Association for the Advancement of Science.
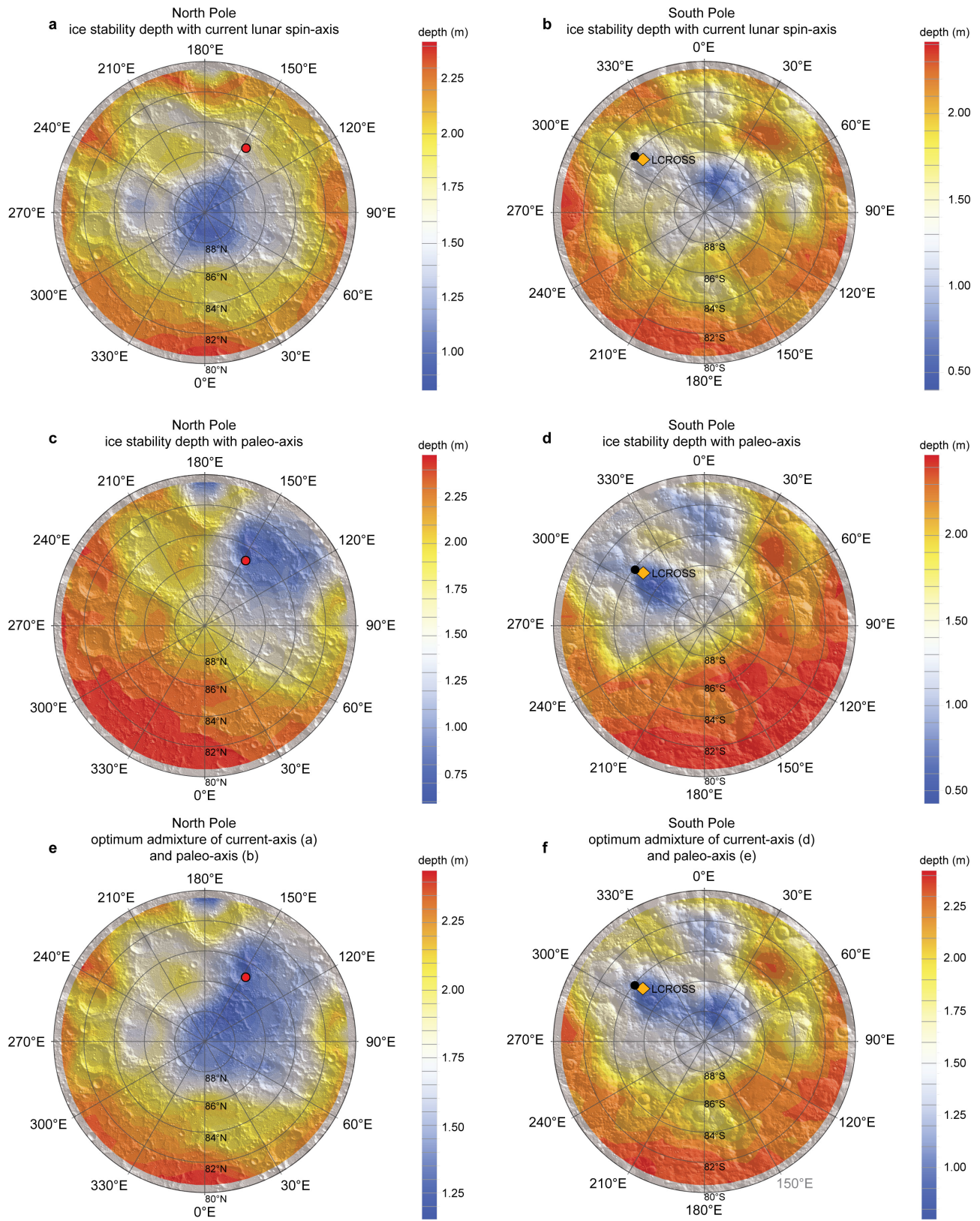
Extended Data Figure 4 | Water-ice stability depths for the past and present poles. a–f, Water-ice stability depths for the north (**a, c, e**) and south (**b, d, f**) polar regions. The model-derived stability depths[4–6] are shown for the current lunar spin axis (**a, b**) and the hypothesized palaeo-axis (**c, d**). Also shown is the optimum admixture of current- and palaeo-axis models that best matches the distributions of polar hydrogen abundance (**e, f**). Topography measured by the LOLA instrument[29] has been superimposed. Latitudinal contours are every 2° poleward of 80°. All other symbols are defined in Fig. 1.
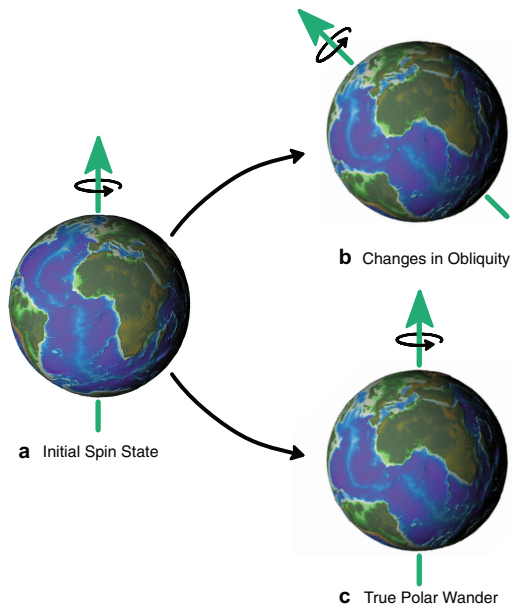
Extended Data Figure 5 | Two different modes of planetary reorientation. a–c, Initial spin state (**a**), changes in obliquity (**b**) and changes due to TPW (**c**). In these schematics, we view the reorienting planet in an inertial frame.

**a** Initial Spin State

b Changes in Obliquity

c True Polar Wander
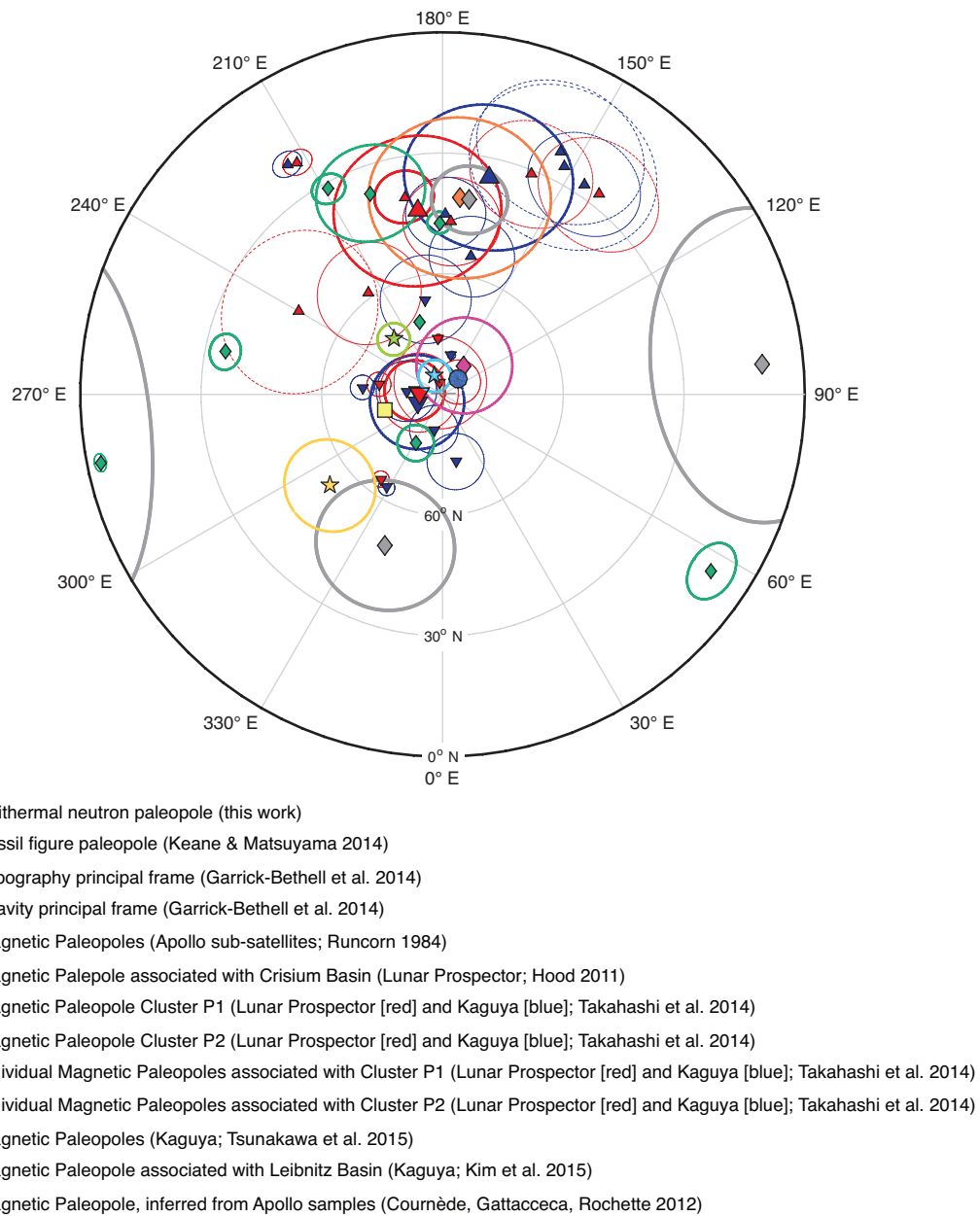
Extended Data Figure 6 | The Moon's many published palaeopoles. A collection of all published lunar palaeopoles, from a combination of palaeomagnetic data (diamonds[60,61,63,64], triangles[19] and square[62]), fossil figure estimates (stars[20,21]) and the epithermal neutron palaeopole reported here (circle). Ellipses around each point indicate 1σ error.
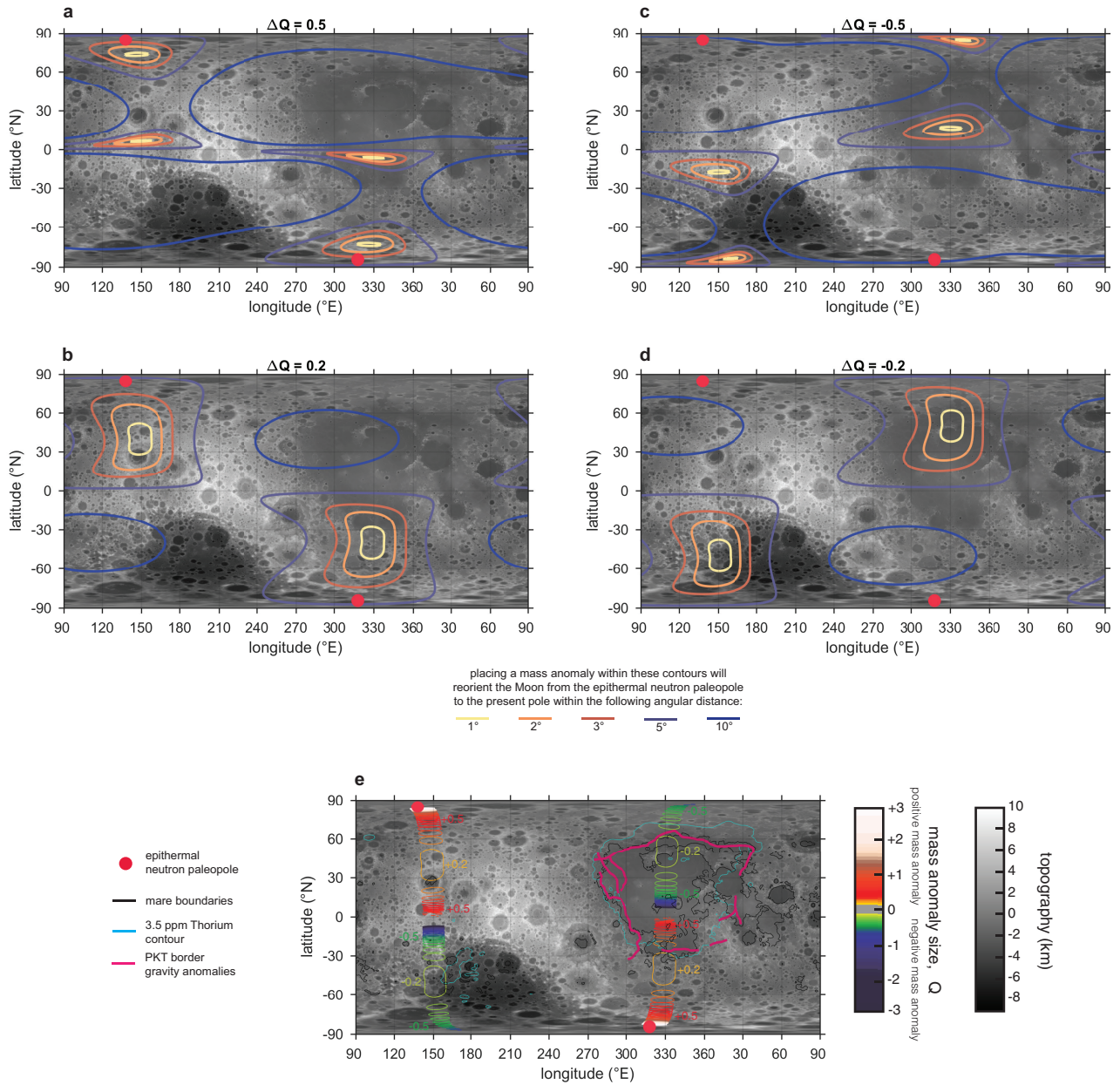
Extended Data Figure 7 | Slices through the mass-anomaly parameter-space search. a–d, Coloured contours enclose regions where placing a mass anomaly ΔQ of the indicated size will cause a reorientation of the Moon to within the specified distance (see legend) of the present-day lunar spin pole. Red filled circles denote the epithermal neutron palaeopole.

e, Contours enclose regions where mass anomalies ΔQ must be centred to reorient the Moon from the epithermal neutron palaeopole to the present-day spin pole, to within 1°. This figure is the same as in Fig. 3a–c, but in an equirectangular projection; symbols and lines as in Fig. 3a–c.
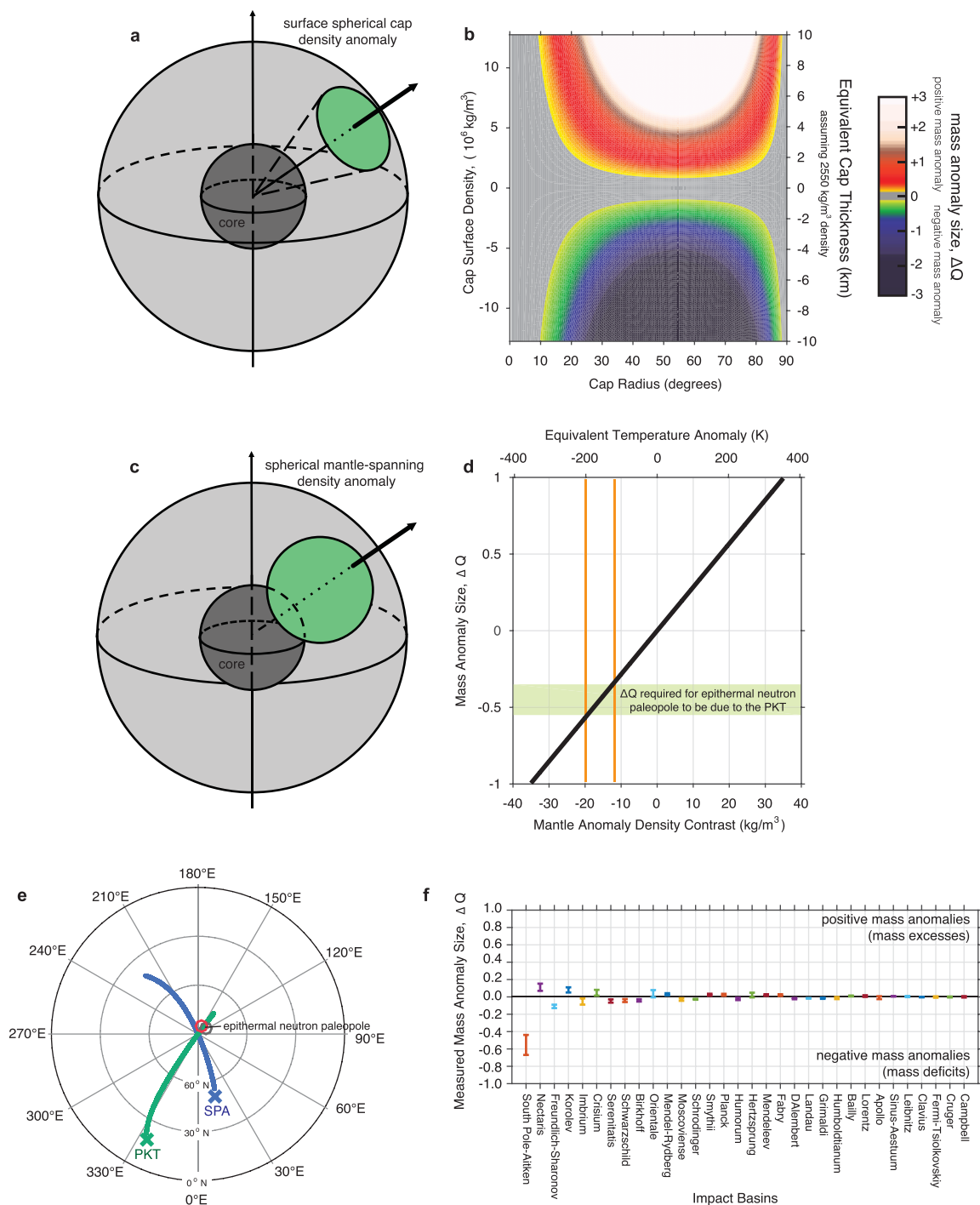
Extended Data Figure 8 | Simple physical models for reorienting the Moon, and the effect of lunar impact basins. a, A schematic of our spherical cap model, showing a spherical cap on the surface of the Moon (green circle), centred on a particular latitude and longitude (arrow). **b**, The mass anomaly ΔQ for a spherical cap as a function of cap size and cap surface density (or cap thickness, assuming a density of $\rho = 2{,}550\,\mathrm{kg\,m^{-3}}$). **c**, A schematic of our mantle-spanning interior anomaly, with a spherical mass anomaly (green circle), centred on a particular latitude and longitude (arrow), grazing the core (dark grey circle) and the surface. **d**, The mass anomaly ΔQ for the spherical mantle anomaly as a function of the density contrast of the anomaly (black line). Over-plotted (green shading and orange lines) is the ΔQ required if the

PKT is responsible ($\Delta Q = -0.45$; Fig. 3c). **e**, North polar projection of all possible palaeopole positions based on a mass anomaly placed at either the PKT or South Pole–Aitken basin (SPA). PKT paths always pass through the neutron palaeopole, whereas SPA paths are nearly orthogonal to this path. **f**, Mass anomalies ΔQ of the largest lunar impact basins derived from inverse fitting of the present-day lunar gravity field, following the method outlined in ref. 21. The only impact basin with a large enough mass anomaly is the South Pole–Aitken basin, which is not properly located to drive the observed TPW (Fig. 3b). The only major impact basin that is properly located is Moscoviense, which has a negligible mass anomaly (and with the wrong sign). Error bars are 1σ uncertainties from the inverse solution (see ref. 21).
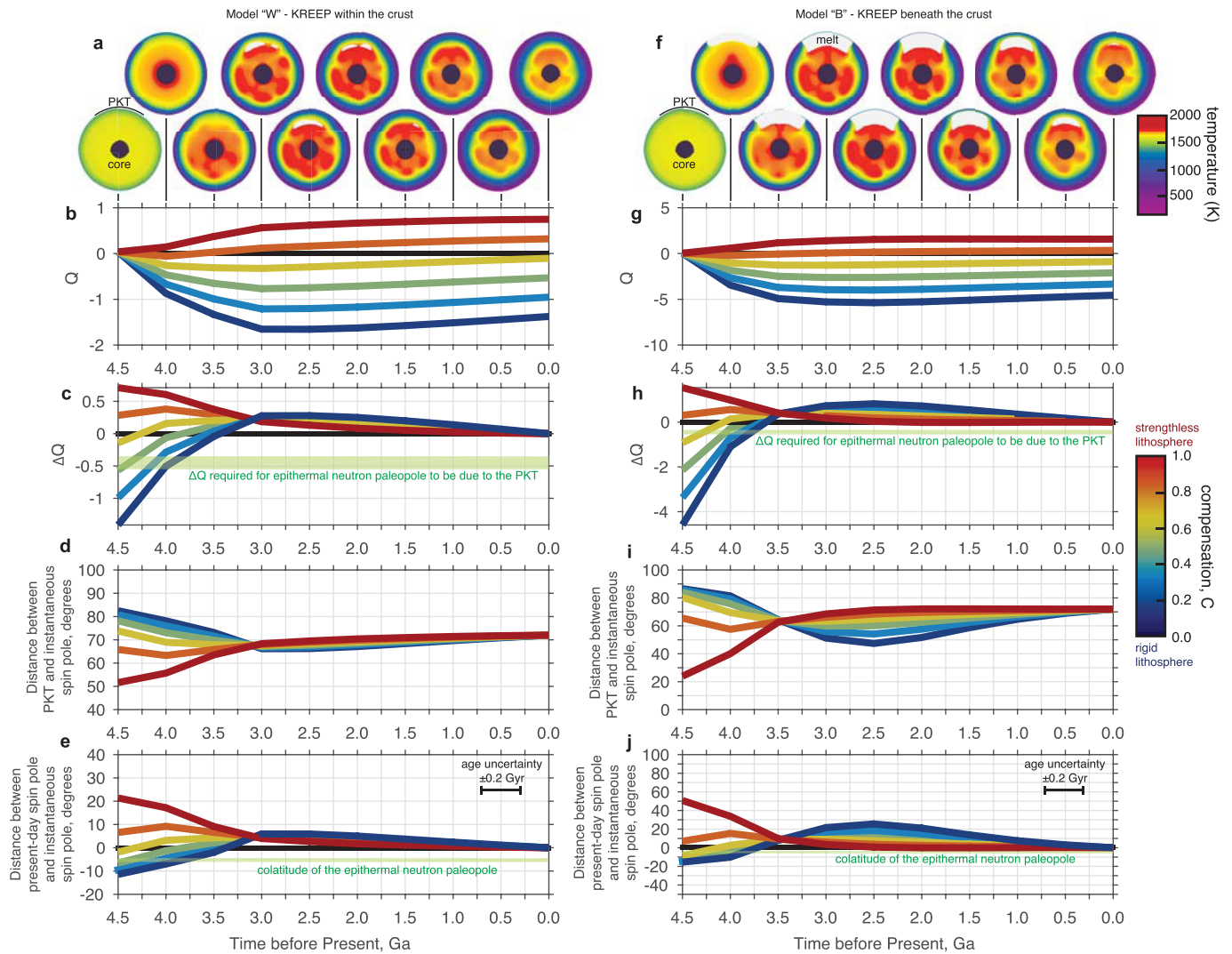
Extended Data Figure 9 | Mass anomalies and TPW of the Moon due the thermal evolution of the PKT. a–e, Results for model W, in which KREEP is mixed within the crust. **f–j,** Results for model B, in which KREEP is mixed beneath the crust. **a, f,** Temperature cross-sections of the lunar mantle, as a function of time. The dark circle is the lunar core. White regions are partially molten. **b, c, g, h,** The mass anomaly Q (**b, g**) and ΔQ (**c, h**) associated with the thermal anomalies shown in **a** and **f**, respectively, as functions of time for various assumed compensation states (coloured lines). $C = 0$ corresponds to a rigid lithosphere; $C = 1$ corresponds to a strengthless lithosphere. The region required to explain the epithermal neutron palaeopole is highlighted in green. **d, i,** The distance between PKT and the instantaneous spin pole as a function of time. **e, j,** The co-latitude of the instantaneous spin pole as a function of time. In this plot, the co-latitude is defined as positive if the northern spin pole is on the near side and negative if it is on the far side. The co-latitude of the epithermal neutron palaeopole is highlighted in green.
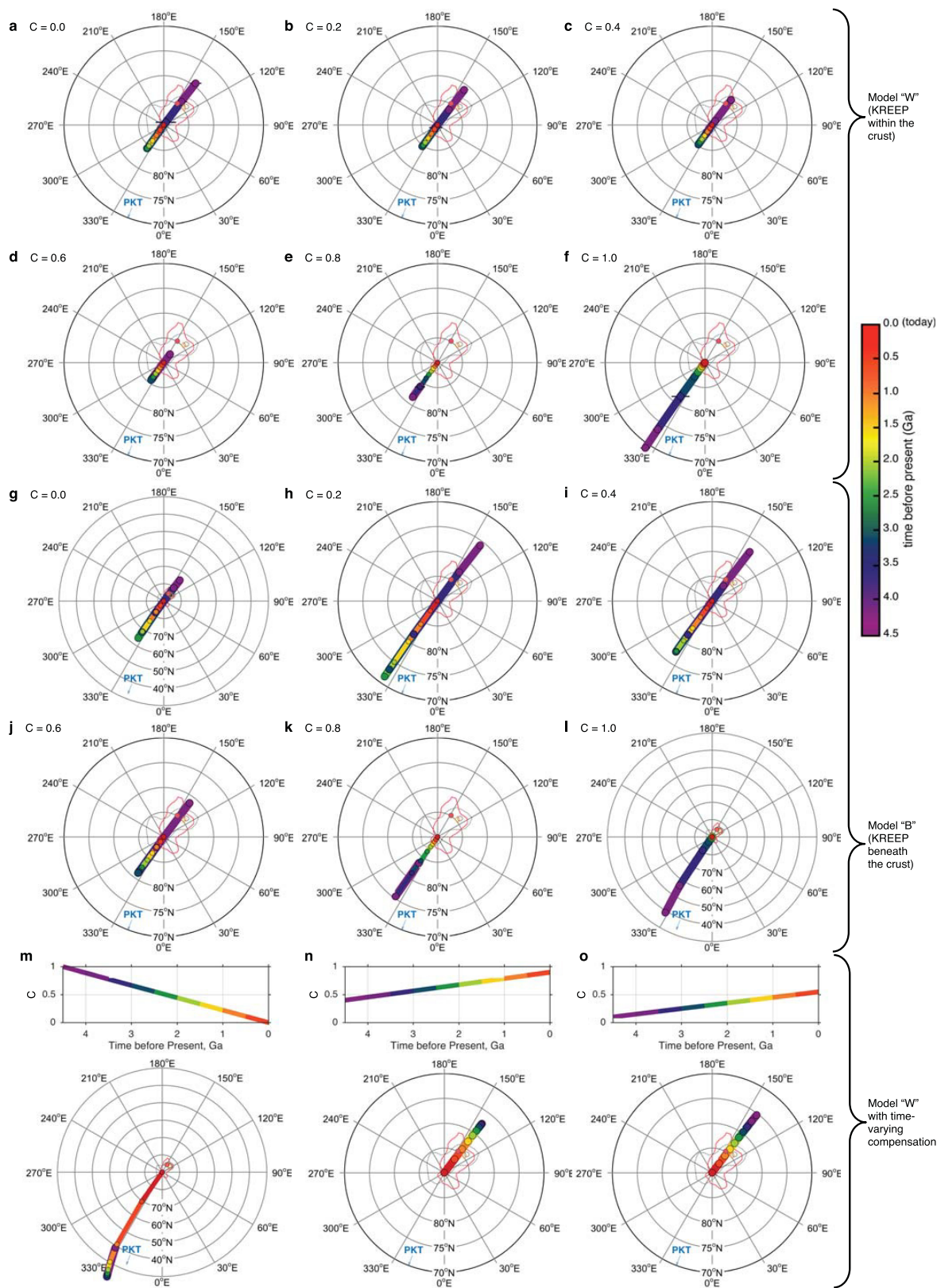
Extended Data Figure 10 | Predicted TPW paths due to the thermal evolution of the PKT for a range of models and compensation states. a–f, Model W, in which KREEP is mixed within the crust; **g–l**, model B, in which KREEP is mixed beneath the crust; **m–o**, model W, with a time-varying compensation state. In general, these TPW paths are consistent with the epithermal neutron pole forming early (4 ± 0.5 Gyr ago), as long as the lithosphere is partially rigid. If the lithosphere is weak or strengthless (**d–f**, **k**, **l**), the topographic uplift from the PKT thermal anomaly dominates and the TPW track never passes through the epithermal neutron pole.

m, An example where the lithosphere starts strengthless (fluid; $C = 1$) and becomes perfectly rigid ($C = 0$) by the present day. **n, o**, Examples where the lithosphere starts partially rigid and becomes weaker with time. Although these cases may not be geophysically feasible, it is interesting as it confines the TPW paths to within the observed hydrogen distribution and reduces the age of the epithermal neutron palaeopole. Error bars indicate 1σ uncertainty in the palaeopole position due to the rotational ambiguity of the PKT thermal models; the error bars are often smaller than the plotted pole positions. Contours and symbols as in Fig. 2a.

Author Queries

Query Reference	Query
1	AUTHOR: This PDF proof has been produced on the basis of your corrections to the preproof and contains the main-text figures edited by us and the Extended Data items supplied by you (which may have been resized but will not have been edited otherwise by us).
	When you receive the PDF proof, please check that the display items are as follows (doi:10.1038/nature17166): Figs 1,2,3,4 (colour); Tables, none; Boxes, none; Extended Data display items, 10 figures; SI, yes.
	Please check the edits to all main-text figures very carefully, and ensure that any error bars in the figures are defined in the figure legends. If you wish to revise the Extended Data items for consistency with main-text figures and tables, please copy the style shown in the PDF proof (such as italicising variables and gene symbols, and using initial capitals for labels) and return the revised Extended Data items to us along with your proof corrections.
2	AUTHOR: My apologies for the error in the citations. At this stage of the production process, I think it is better to leave the citation to ref. 57 out of order, rather than rerenumbering the references, which could potentially introduce further errors; ok?
3	AUTHOR: Thank you for pre-emptively shortening the heading; I've left this query here to remind us to double check this and the other headings on the proof for length.
4	AUTHOR: Script R sounds like a great solution; thanks!
5	AUTHOR: I changed $\mathcal{R}^{-1}$ (in your preproof corrections) back to $\mathcal{R}^{\top}$ to match your original submission and the usual notation for transpose; please edit if '-1' as a superscript was correct.
Web summary	Polar hydrogen deposits on the Moon provide evidence that its spin axis has shifted; analysis of the locations of these deposits and of the lunar figure suggests that the shift occurred as a result of changes in the Moon's moments of inertia caused by a low-density thermal anomaly beneath the Procellarum region.

For Nature office use only:

Layout	☐	Figures/Tables/Boxes	☐	References	☐
DOI	☐	Error bars	☐	Supp info	☐
Title	☐	Colour	☐	Acknowledgements	☐
Authors	☐	Text	☐	Author contribs	☐
Addresses	☐	Methods	☐	COI	☐
First para	☐	Received/Accepted	☐	Correspondence	☐
		AOP	☐	Author corrx	☐
		Extended Data	☐	Web summary	☐
				Accession codes link	☐